

# Mobile-to-Mobile Uncorrelated Scatter Channels

Michael Walter<sup>1</sup>, Senior Member, IEEE, Martin Schmidhammer<sup>1</sup>, Senior Member, IEEE,  
Miguel A. Bellido-Manganell<sup>1</sup>, Thomas Wiedemann<sup>1</sup>, Member, IEEE,  
and Dmitriy Shutin<sup>1</sup>, Senior Member, IEEE

**Abstract**—In this paper, we present a complete analytic probability based description of mobile-to-mobile uncorrelated scatter channels. We provide a theoretical proof that the proposed probability based description is equivalent to the correlation based description introduced by Bello and Matz. This equivalence is evaluated through a comparison of the hybrid characteristic probability density function with the correlation based description of a measured generic mobile-to-mobile channel, both of which can be obtained directly either from theory or from measurement data. The comparison confirms the similarity between the probability based and correlation based description qualitatively and quantitatively. Thus, the proposed probabilistic description complements the common correlation based description providing a comprehensive theoretical description of arbitrary uncorrelated scatter channels.

**Index Terms**—Doppler frequency, mobile-to-mobile communications, geometry based stochastic channel model, hybrid characteristic probability density function, prolate spheroidal coordinate system, non-stationary channels.

## I. INTRODUCTION

THE significance of mobile-to-mobile (M2M) communications is progressively growing. Especially vehicle-to-vehicle (V2V) communications – just one area of modern M2M communications – is becoming increasingly integrated into newly manufactured cars to mitigate possible accidents via situational awareness. Moreover, it will become an integral part of future autonomous driving vehicle solutions [1]. Similar direct communication frameworks are envisioned for various modes of transportation such as trains, ships, aircraft, and drones. Historically, the channel models used for the design and testing of communication systems in the past were wide-sense stationary uncorrelated scattering (WSSUS). They were largely valid as they were mainly for fixed-to-mobile channels. However, they are inadequate in an M2M context due to the inherent non-stationarity and uncorrelated scattering characteristics of the channel.

Scattering is ultimately a stochastic process. It has been shown in [2] and [3] that it can be well explained by means of postulating a power spectral density in the frequency domain, or equivalently with an autocorrelation function in the

temporal domain. Temporal stochastic variations can also be described in a similar statistical fashion. Clarke derived in [4] a model that describes the Doppler spectrum of the propagation channel in the case of a mobile receiver, e.g., a moving car communicating with a fixed base station. This type of Doppler spectrum is widely known as Jakes spectrum [5]. In [6] Bello extended the mentioned models to more general channels, describing statistical characterizations for both WSSUS and non-WSSUS channels. M2M model extensions for various two-dimensional (2D) and three-dimensional (3D) scenarios are presented in [7] and [8]. Later, Matz in [9] focused on non-WSSUS channels, which he studies from two complementary perspectives. First, the time frequency channel transfer function can be treated as a non-stationary process in both time and frequency domains. Second, by assuming that scatterers with distinct delays and Doppler frequencies are uncorrelated, the resulting channel impulse response can be studied as non-stationary in time and uncorrelated along the delay. This allows to introduce the local scattering function (LSF) and the channel correlation function (CCF), which both describe small-scale channel statistics. The two functions are naturally related to correlation functions introduced by Bello in [6] via Fourier transforms.

Bello states in Section IV of his seminal work [6] that it's difficult to find an exact statistical description of a time-variant channel in terms of multidimensional probability functions and that correlation functions are a more practical approach. This statement implies that without further physical assumptions on the propagation environment, an accurate statistical characterization of non-WSSUS channels can be quite elusive. It thus motivates the application of geometric-stochastic modeling approaches, where a specific propagation geometry is assumed, or at least some additional assumptions on the structure of the channel are put into place.

One such approach is exemplified well in [10]. It reveals that M2M channels typically violate the wide-sense stationary (WSS) assumption to a greater extent than the uncorrelated scattering (US) assumption. This, on the one hand, constrains general non-WSSUS type of channels to more restricted cases, while on the other hand, building a highly relevant application scenario for the design of practical M2M communication systems. Our objective in this paper is therefore to explore such non-WSS channels in more detail, providing a common probability based characterization describing the non-stationary behavior of arbitrary M2M channels. The main contributions of the paper are the following. We

- provide a complete probability based description of non-stationary M2M channels,

Received 22 July 2024; revised 12 December 2024; accepted 12 February 2025. This work was supported by the DLR internal project GNSS Technologien und Dienste. The associate editor coordinating the review of this article and approving it for publication was C. Han. (Corresponding author: Michael Walter.)

The authors are with the Institute of Communications and Navigation, German Aerospace Center (DLR), 82234 Wessling, Germany (e-mail: m.walter@dlr.de; martin.schmidhammer@dlr.de; miguel.bellidomanganell@dlr.de; thomas.wiedemann@dlr.de; dmitriy.shutin@dlr.de).

Code is available online at <https://codeocean.com/capsule/7991892/tree/v1>. Digital Object Identifier 10.1109/TWC.2025.3542478

- complement and highlight the relation of the probability based description to the correlation based description by Bello [6] and Matz [9],
- show a general proof for the equivalence of probability based and correlation based descriptions,
- define hybrid characteristic probability density functions,
- validate the theoretical probability based description through a comparison with measurement data.

In detail, we extend the proof of the proportionality between the joint delay Doppler probability density function (pdf) and scattering function for the WSSUS case in [11] and [12] to non-WSS channels by using the time-variant time frequency correlation function shown in [13]. We present the hybrid characteristic probability density function in order to enable a direct comparison of a theoretically computed, closed-form probability based function with a correlation based description evaluated from measurement data. A similar concept of a hybrid characteristic pdf was introduced in [14] to describe multivariate pdfs, where an inverse Fourier transform was applied only over one of the variables, resulting in a mixture of a pdf and a characteristic function.

Since the correlation based description only allows for an analysis after the measurement, our probability based description enables the prediction and simulation of arbitrary M2M channels by only relying on the geometry of the propagation scenario. Being able to theoretically describe high mobility M2M channels allows to validate emerging technologies in radio communications including new modulation schemes like orthogonal time frequency space (OTFS) [15], [16], or integrated sensing and communications (ISAC) as in [17].

The remainder of the paper is structured as follows. In Section II, we provide a complete stochastic description of the uncorrelated M2M channel and relate those functions to the correlation functions, LSF, and CCF. In Section III, we show, how the hybrid time delay characteristic probability density function is calculated in closed form. The equivalence of the theoretical probability based description is then verified by the correlation based evaluation of measurement data from an aircraft-to-aircraft measurement campaign in Section IV. The paper is concluded with Section V.

## II. CHARACTERIZATION OF US CHANNELS

In order to obtain analytical solutions for the probability based description, it is essential to establish a unified mathematical framework. Our goal is to establish connections between the models developed by Bello in [6] and Matz in [9] with our probabilistic approach.

Consider a classical communication channel between a transmitter (TX) and receiver (RX), both possibly mobile. The relationship between the transmitted signal  $s(t)$  and the received signal  $r(t)$  can be represented as [9]

$$r(t) = \int h(t, \tau) s(t - \tau) d\tau, \quad (1)$$

where the function  $h(t, \tau)$  – the time-variant channel impulse response – fully characterizes the propagation environment between the TX and the RX and where  $t$  is the absolute time and  $\tau$  the delay. Essentially (1) states that the received

signal is a superposition of differentially delayed copies of the transmitted signal. The channel can be defined in terms of the spreading function or also known as Doppler-variant impulse response  $S(\tau, \nu) = \int h(t, \tau) e^{-j2\pi\nu t} dt$ , the time-variant transfer function  $L(t, f) = \int h(t, \tau) e^{-j2\pi f\tau} d\tau$ , via a Fourier transform over the delay variable  $\tau$  or the Doppler-variant transfer function  $T(\nu, f) = \int \int h(t, \tau) e^{-j2\pi\nu t} e^{-j2\pi f\tau} dt d\tau$ , which is obtained by a double Fourier transform of  $h(t, \tau)$  over  $t$  and  $\tau$ . The variable  $f$  denotes the frequency and  $\nu$  the Doppler frequency shift. Knowledge of  $h(t, \tau)$ , or any of the other three functions is thus instrumental for the design, simulation, or testing of practical communication systems.

### A. Correlation Based Description

In practice, an exact form of  $h(t, \tau)$  depends on the particular propagation environment. The environment, however, is rarely known accurately or in advance at the stage of communication system design. Therefore, as has been mentioned earlier, statistical properties of  $h(t, \tau)$  are of interest. Similarly, the statistical properties of the other three system functions  $S(\tau, \nu)$ ,  $L(t, f)$ , and  $T(\nu, f)$  can be determined. These statistics can be captured by the corresponding auto-correlation functions of the four system functions according to [6], [9], and [18] as

$$\begin{aligned} R_h(t, \tau; \Delta t, \Delta \tau) &= \mathbb{E}\{h(t, \tau + \Delta \tau) h^*(t - \Delta t, \tau)\}, \\ R_L(t, f; \Delta t, \Delta f) &= \mathbb{E}\{L(t, f + \Delta f) L^*(t - \Delta t, f)\}, \\ R_S(\tau, \nu; \Delta \tau, \Delta \nu) &= \mathbb{E}\{S(\tau, \nu + \Delta \nu) S^*(\tau - \Delta \tau, \nu)\}, \\ R_T(\nu, f; \Delta \nu, \Delta f) &= \mathbb{E}\{T(\nu, f + \Delta f) T^*(\nu - \Delta \nu, f)\}. \end{aligned} \quad (2)$$

Here the operator  $\mathbb{E}\{\cdot\}$  denotes the expectation operation,  $(\cdot)^*$  the complex conjugate, and  $R(\cdot, \cdot; \cdot, \cdot)$  is the autocorrelation function.<sup>1</sup> By taking double Fourier transforms of the correlation functions, a set of four equivalent, yet different descriptions of the channel can be obtained.

One can see that the correlation functions in (2) are four-dimensional (4D) functions. These functions are difficult to work with, not to mention hard to get insights into or intuition about their properties. To simplify the analysis, one can often invoke the WSSUS assumption, see e.g., [6]. Its consequence is that correlation functions in (2) become dependent only on the corresponding time and frequency lag variables. They thus collapse to much simpler 2D functions, see [6] and [9]. Due to this simplification, the WSSUS assumption has dominated channel modeling over decades, especially for non-mobile applications or fixed-to-mobile (F2M) channels, i.e., with a fixed base station. Yet, the mobility of TX and RX nowadays brings in the non-stationarity of the propagation environment, and thus of the channel. In [9] the LSF was introduced as an alternative second-order channel statistic to account for non-stationarities in the time and frequency domains. The LSF generalizes the scattering function for non-WSSUS channels, but, as mentioned above, it is a 4D function. Many M2M channels, however, in particular V2V channels, are non-stationary,

<sup>1</sup>Due to the equivalence of the expectancy operators  $\mathbb{E}\{f(x, y + \Delta y) f^*(x - \Delta x, y)\} = \mathbb{E}\{f(x, y) f^*(x - \Delta x, y - \Delta y)\} = \mathbb{E}\{f(x + \Delta x, y + \Delta y) f^*(x, y)\}$ , the expressions in (2) can be modified correspondingly.

yet preserve the US property. This permits describing US channels with only three variables instead of four.

According to [6], US channels were observed for troposcatter communication and moon reflections. Recently, similar effects were also observed for M2M channels, where the uncorrelated scattering assumption was validated with measurements, see e.g., [10]. There the author states that the V2V channel infringes the WSS assumption much stronger than the US assumption. In the US case the scatterers can be modeled as a continuum of uncorrelated scatterers according to [6]. As a result, the general correlation functions in (2) become independent of  $\Delta\tau$ , since the correlation between scatterers causing different delays vanishes. Under the US assumption (2) can be represented, see also [6, (64)-(66)], as<sup>2</sup>

$$\begin{aligned} R_h(t, \tau; \Delta t, \Delta\tau) &= P_h(t; \tau, \Delta t) \delta(\Delta\tau), \\ R_L(t, f; \Delta t, \Delta f) &= R_L(t; \Delta t, \Delta f), \\ R_S(\tau, \nu; \Delta\tau, \Delta\nu) &= P_S(\tau, \nu; \Delta\nu) \delta(\Delta\tau), \\ R_T(\nu, f; \Delta\nu, \Delta f) &= R_T(\nu; \Delta\nu, \Delta f), \end{aligned} \quad (3)$$

where  $\delta(\cdot)$  is the Dirac delta distribution and  $P_h(t; \tau, \Delta t)$  and  $P_S(\tau, \nu; \Delta\nu)$  are cross-power spectral densities. Using  $P_h$  from (3), the time-variant LSF is defined [19] as

$$\mathcal{C}_H(t; \tau, \nu) = \int P_h(t; \tau, \Delta t) e^{-j2\pi\Delta t\nu} d\Delta t. \quad (4)$$

Furthermore, in [9] Matz defines the corresponding channel correlation function, which we simplify here to

$$\mathcal{A}_H(\Delta t, \Delta f; \Delta\nu) = \int R_L(t; \Delta t, \Delta f) e^{-j2\pi\Delta\nu t} dt, \quad (5)$$

which brings the total available functions to describe the US channel statistically to six, which are given in (3), as well as (4) and (5). The reduction of dimensionality of the six correlation based functions permits simpler visualization and interpretation, which in turn provide valuable insights into the correlation properties of the channel.

Again, the resulting correlation functions can be studied both in time, time lag, or frequency and frequency lag domains. As a consequence, for the 3D functions in (3) a total of eight equivalent representations can mathematically be established. However, in [6] Bello discusses only the four proper correlation functions, where the time and frequency variables, as well as the associated lag variables are in the same domain, e.g. either both in the temporal or both in the frequency domain. Later in [9] Matz proposed the time-variant LSF and the channel correlation function, which are obtained by Fourier transforms of the original four correlation functions as shown in (4) and (5). As we will see, it is also useful to consider the correlation variables in a mixed temporal frequency domain, thus extending the available six functions from Bello and Matz to a total of eight. All these functions are summarized conceptually in Table I, where they are related to their probabilistic based counterparts as shown in the next subsection.

<sup>2</sup>Note that equations in (3) imply that the right-hand side is independent of  $f$  in case of the US assumption.

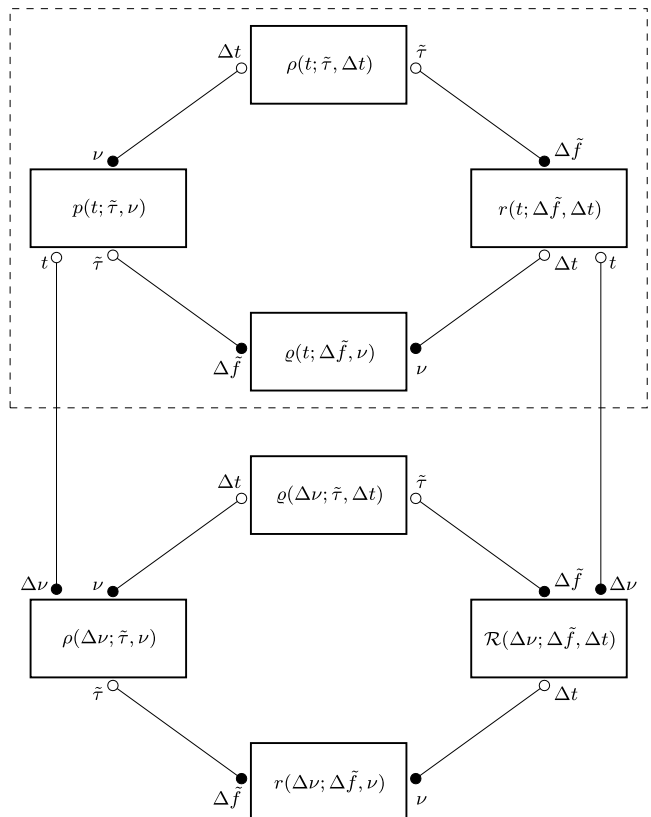


Fig. 1. Time-variant and Doppler correlated relationships between characteristic functions, probability density functions, and hybrid characteristic probability density functions for the US channel. Time-variant functions, which are referred to in Fig. 2, are framed by a dashed rectangle. Fourier transforms are indicated by the  $\circ \rightarrow \bullet$  sign.

In order to set all correlation based functions in a relationship with the probability based functions discussed later, we need to make a new definition. Thus, we define

$$P_\varrho(t; \Delta f, \nu) \triangleq \int \mathcal{C}_H(t; \tau, \nu) e^{-j2\pi\Delta f\tau} d\tau, \quad (6)$$

as the Fourier transform of the time-variant LSF with respect to the delay variable  $\tau$ .

### B. Probability Based Description

In this subsection, we discuss the probabilistic representation of the US channel more formally. We begin by defining  $\tilde{\tau} \triangleq \tau/\tau_{\text{LOS}}$  as the normalized delay, where  $\tau_{\text{LOS}}$  is the line-of-sight (LOS) delay between the TX and RX. Similarly, we define the normalized frequency lag  $\Delta \tilde{f} \triangleq \Delta f \tau_{\text{LOS}}$ . In the following, we will combine the notation common in channel modeling literature with our previous works, e.g., [20], where the focus was on deriving the joint delay Doppler pdf  $p(t; \tilde{\tau}, \nu)$  for the M2M channel.

Note that by taking Fourier transforms along some of the variables of these functions, we obtain equivalent representations, yet in the corresponding frequency domains. This will allow for other, often quite revealing, interpretations of the channel properties, as will be shown later. These different transforms are shown for the US case in Fig. 1. Of particular interest is the time-variant joint delay Doppler pdf  $p(t; \tilde{\tau}, \nu)$

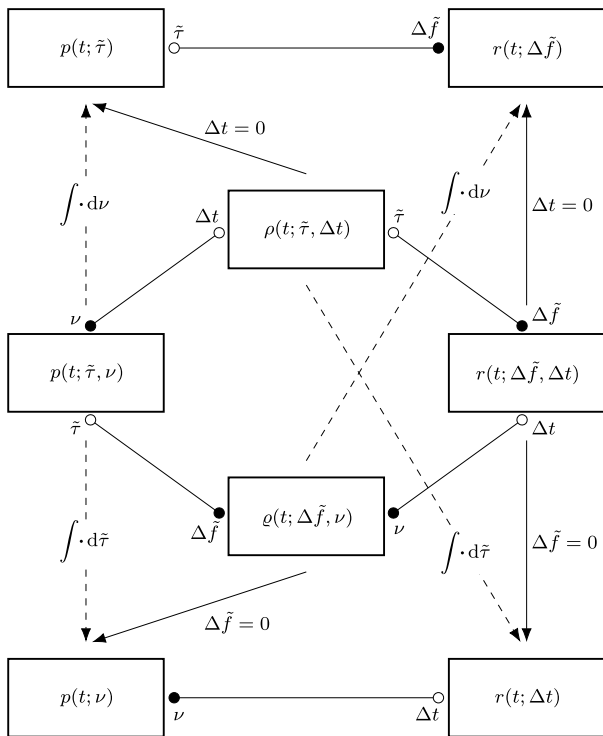


Fig. 2. Time-variant relationships between characteristic functions, probability density functions, and hybrid characteristic probability density functions for the US channel. Fourier transforms are indicated by the  $\circ \rightarrow$  sign, integrals by  $\dashrightarrow$ , and setting the  $\Delta$  variable to zero by  $\rightarrow$ .

that we introduced before in [20]. The time-variant joint delay Doppler pdf  $p(t; \tilde{\tau}, \nu)$  can be computed analytically, e.g., for M2M US channels. Furthermore, it has a finite support, since the velocity and sensitivity limit the possible delays and Doppler frequencies. Since the trajectories of TX and RX are time-variant, it makes sense to use a time-variant probability density. In our case the time  $t$  is a deterministic variable, whereas the delay  $\tilde{\tau}$  and Doppler frequency  $\nu$  are treated as stochastic variables. Their distributions are obtained from the assumption that scatterers are uniformly distributed on the ground. This is followed by a variable transform from the spatial to the Doppler domain, see [20]. To illustrate the connection between the correlation functions from [6] and their equivalent forms in [9], we summarize them in Table I, using the original notation of the references.

Our objective is to relate the joint delay Doppler pdf  $p(t; \tilde{\tau}, \nu)$  [20] to the LSF [9] and, what we call, the hybrid characteristic pdf  $\rho(t; \tilde{\tau}, \Delta t)$  to the delay cross-power spectral density in [6]. Recall that for the joint pdfs this is equivalent to computing the characteristic function for one of the two variables. Thus,  $\rho(t; \tilde{\tau}, \Delta t)$  is a characteristic function along the  $\Delta t$  direction and a pdf along the delay direction. Accordingly, this function presents a time-variant spectral density along the  $\tilde{\tau}$  variable and a temporal correlation along the  $\Delta t$  variable. Such a hybrid characteristic pdf has been originally introduced in [14] and can be factored as

$$\rho(t; \tilde{\tau}, \Delta t) = p(t; \tilde{\tau})\rho(t; \Delta t | \tilde{\tau}). \quad (7)$$

Since M2M channels are non-stationary, this function is particularly useful, since it allows observing a time-variant,

delay-dependent temporal correlation of the channel. Using Fourier transforms to convert the time or frequency variables will lead to other hybrid representations of the channel, where the function represents a characteristic function along one of the variables and a probability density along the other. Thus, we consider the Fourier and inverse Fourier transform as basically the same operation, but with different signs. In Fig. 1 this is represented with functions, e.g.,  $\rho(t; \tilde{\tau}, \Delta t)$  and  $\varrho(t; \Delta \tilde{f}, \nu)$ , which are neither pure characteristic nor probability density function representations.

For an easier comparison to WSSUS channels, the eight functions in Fig. 1 can be partitioned into (i) a time-variant (dashed box) and (ii) a Doppler correlated description. We consider time-variant descriptions as more natural and easier to interpret, although all descriptions enjoy an equivalence under the appropriate Fourier transform. The reasoning behind this lies in the fact that in M2M scenarios both TX and RX move, resulting in time-variant velocity vectors. Thus, a time-variant channel description would be more natural. Yet, via appropriate Fourier transform we can equivalently obtain Doppler correlated descriptions – the lower part of Fig. 1. These are, however, less intuitive to interpret.

1) *Time-Variant Functions*: We begin with the known time-variant joint delay Doppler pdf  $p(t; \tilde{\tau}, \nu)$  from [20] as a starting point for further analysis. An inverse Fourier transform along the Doppler variable leads to a hybrid characteristic pdf representation, as we mentioned above. Let us consider the joint delay Doppler pdf  $p(t; \tilde{\tau}, \nu)$  and the corresponding hybrid representation

$$\rho(t; \tilde{\tau}, \Delta t) \triangleq \int p(t; \tilde{\tau}, \nu) e^{j2\pi\nu\Delta t} d\nu. \quad (8)$$

It is important to note that  $\rho(t; \tilde{\tau}, \Delta t = 0) = p(t; \tilde{\tau})$ , since (8) becomes a marginalization integral then. Indeed, by setting the characteristic variable  $\Delta t$  to zero, the exponential function in the integral vanishes, and the marginal, time-variant pdf  $p(t; \tilde{\tau})$  can be obtained. This time-variant delay pdf is proportional to  $P_h(t; \tilde{\tau}, \Delta t = 0)$ , which is the power delay profile of the channel, see Theorem 1. Thus, we have a non-parametric, geometry based, time-variant path loss model, which we will analytically derive for the general M2M channel. With the time-variant delay pdf  $p(t; \tilde{\tau})$  we can obtain the factorization of the time-variant, delay-dependent Doppler probability density as  $p(t; \tilde{\tau}, \nu) = p(t; \tilde{\tau})p(t; \nu | \tilde{\tau})$ , which reveals the conditional density  $p(t; \nu | \tilde{\tau})$ , i.e., the Doppler pdf conditioned on a particular delay  $\tilde{\tau}$ .

With the time-variant pdf  $p(t; \tilde{\tau})$  the hybrid characteristic pdf can also be factorized to a delay-dependent characteristic function. It can be shown as in [14] that with (7) the characteristic function of a conditional pdf can be computed as

$$\begin{aligned} \rho(t; \Delta t | \tilde{\tau}) &= \int p(t; \nu | \tilde{\tau}) e^{j2\pi\nu\Delta t} d\nu \\ &= \frac{\rho(t; \tilde{\tau}, \Delta t)}{\rho(t; \tilde{\tau}, \Delta t = 0)} = \frac{\rho(t; \tilde{\tau}, \Delta t)}{p(t; \tilde{\tau})}. \end{aligned} \quad (9)$$

The other hybrid characteristic pdf contains a pdf in the Doppler domain and a characteristic function in the frequency domain, but here the time and Doppler frequency are in

different domains. The function is given by

$$\varrho(t; \Delta \tilde{f}, \nu) \triangleq \int p(t; \tilde{\tau}, \nu) e^{-j2\pi \Delta \tilde{f} \tilde{\tau}} d\tilde{\tau}. \quad (10)$$

Note that we perform a normal Fourier transform here instead of an inverse one for a characteristic function in order to be consistent with channel modeling literature. Similarly, by setting  $\Delta \tilde{f} = 0$  in (10), we obtain  $\varrho(t; \Delta \tilde{f} = 0, \nu) = p(t; \nu)$ , i.e., the time-variant Doppler probability density. The conditional characteristic function is obtained by

$$\begin{aligned} \varrho(t; \Delta \tilde{f} | \nu) &= \int p(t; \tilde{\tau} | \nu) e^{-j2\pi \Delta \tilde{f} \tilde{\tau}} d\tilde{\tau} \\ &= \frac{\varrho(t; \Delta \tilde{f}, \nu)}{\varrho(t; \Delta \tilde{f} = 0, \nu)} = \frac{\varrho(t; \Delta \tilde{f}, \nu)}{p(t; \nu)}. \end{aligned} \quad (11)$$

The time-variant joint characteristic function  $r(t; \Delta \tilde{f}, \Delta t)$  can be directly obtained by a double Fourier transform as

$$r(t; \Delta \tilde{f}, \Delta t) = \int \int p(t; \tilde{\tau}, \nu) e^{-j2\pi(\Delta \tilde{f} \tilde{\tau} - \nu \Delta t)} d\tilde{\tau} d\nu, \quad (12)$$

with the property  $r(t, \Delta \tilde{f} = 0, \Delta t = 0) = 1$ . Note that in (12) we use one normal and one inverse Fourier transform to compute the joint characteristic function to be consistent with the channel modeling literature. This differs from the description used in [21].

The time-variant mean delay and delay spread can be easily calculated by using the hybrid characteristic pdf and setting  $\Delta t = 0$ . This results in the first two delay moments as

$$\mu_{\tilde{\tau}}(t) = \int_{\tilde{\tau}_{\min}}^{\tilde{\tau}_{\max}} \tilde{\tau} \rho(t; \tilde{\tau}, \Delta t = 0) d\tilde{\tau}, \quad (13)$$

$$\sigma_{\tilde{\tau}}(t) = \sqrt{\int_{\tilde{\tau}_{\min}}^{\tilde{\tau}_{\max}} (\tilde{\tau} - \mu_{\tilde{\tau}}(t))^2 \rho(t; \tilde{\tau}, \Delta t = 0) d\tilde{\tau}}, \quad (14)$$

with  $\tilde{\tau}_{\max} > \tilde{\tau}_{\min} > \tilde{\tau}_{\text{sr}}$  and

$$\tilde{\tau}_{\text{sr}} = \max \left( \sqrt{\frac{A^2 + B^2 + D^2}{A^2 + B^2 + C^2}}, 1 \right), \quad (15)$$

being the delay of the specular reflection relative to the line-of-sight delay. Parameters  $A$ ,  $B$ ,  $C$  and  $D$  are the orientation coefficients of the scattering plane. Their geometric interpretation and computation will be discussed Section III.

If the influence of the delay is removed, we obtain the temporal correlation of the channel per delay. Instead of calculating the total mean Doppler and Doppler spread, we calculate delay-dependent mean Doppler and Doppler spread. These can be obtained from the conditional characteristic function as

$$\begin{aligned} \mu_{\nu | \tilde{\tau}}(t) &= \frac{1}{j2\pi} \frac{\partial}{\partial \Delta t} \rho(t; \Delta t | \tilde{\tau}) \Big|_{\Delta t=0}, \end{aligned} \quad (16)$$

$$\begin{aligned} \sigma_{\nu | \tilde{\tau}}(t) &= \frac{1}{2\pi} \sqrt{\left( \frac{\partial}{\partial \Delta t} \rho(t; \Delta t | \tilde{\tau}) \right)^2 - \frac{\partial^2}{\partial \Delta t^2} \rho(t; \Delta t | \tilde{\tau})} \Big|_{\Delta t=0}, \end{aligned} \quad (17)$$

where  $\rho(t; \Delta t | \tilde{\tau})$  is the inverse Fourier transform of  $p(t; \nu | \tilde{\tau})$  and is therefore a characteristic function in the  $\Delta t$  variable.

2) *Doppler Correlated Functions*: The Doppler correlated functions in Fig. 2 constitute for  $\Delta \nu = 0$  a temporal average of the functions in the upper half. The hybrid Doppler delay characteristic pdf  $\rho(\Delta \nu; \tilde{\tau}, \nu)$  for example is calculated as

$$\rho(\Delta \nu; \tilde{\tau}, \nu) \triangleq \int p(t; \tilde{\tau}, \nu) e^{-j2\pi \Delta \nu t} dt, \quad (18)$$

with  $\rho(\Delta \nu = 0; \tilde{\tau}, \nu)$  being the temporal mean of the joint delay Doppler probability density function due to the Fourier properties. This was already implicitly used in describing V2V scenarios such as two cars driving in opposite directions in [22]. We normalize the functions in such a way, that the joint pdf  $p(t; \tilde{\tau}, \nu)$  is a time-variant probability density in the variables  $\tilde{\tau}$  and  $\nu$ . Thus, the time-variant joint characteristic function  $r(t; \Delta \tilde{f} = 0, \Delta t = 0) = 1$ . The lower half functions with  $\Delta \nu$  deviate from pdfs or characteristic functions by a factor of  $T = 1/\Delta \nu$ . The channel correlation function  $\mathcal{A}_{\mathbf{H}}(\Delta t, \Delta f; \Delta \nu)$  by Matz thus corresponds to  $\mathcal{R}(\Delta \nu; \Delta \tilde{f}, \Delta t)$ . We will focus our attention in the remaining paper on the time-variant functions, since a time-variant joint pdf as a basis of the description seems more natural with time-variant trajectories of TX and RX as input to our model.

Finally, as illustrated in Table I, we note that the probability based functions  $r$  and  $\rho$  correspond to the correlation functions  $R$  and  $P$  of Bello, respectively. Further, the joint pdf  $p$  corresponds to the time-variant LSF  $\mathcal{C}_{\mathbf{H}}$  and triple frequency Doppler time characteristic function  $\mathcal{R}$  to the uncorrelated scatter channel correlation function  $\mathcal{A}_{\mathbf{H}}$ . For completeness, we further present two new hybrid functions  $\varrho$  with mixed variables in both time-variant and Doppler correlated domains.

### C. Proportionality Between the Correlation and Probability Based Functions

The following theorem states that stochastic channel descriptions computed based on the joint delay Doppler pdf, as shown in Fig. 2, are proportional to the corresponding correlation based functions derived by Bello and Matz in their works. Note that the same variables as Matz are used.

*Theorem 1: The autocorrelation of the time-variant transfer function  $R_L(t; \Delta t, \Delta \tilde{f})$  is proportional to the time-variant joint time frequency characteristic function  $r(t; \Delta \tilde{f}, \Delta t)$*

$$R_L(t; \Delta t, \Delta \tilde{f}) \propto r(t; \Delta \tilde{f}, \Delta t).$$

Furthermore, due to the linearity of Fourier transforms, the above stated proportionality applies for each pair of correlation and probability based functions as outlined in Table I.

*Proof:* We follow here the steps similar to those in [11]. The starting point is the assumption that for the time  $t$  the channel can be represented as a linear combination of  $K(t)$  propagation paths

$$h(t, \tau) = \sum_{k=0}^{K(t)-1} \alpha_k(t) e^{-j2\pi f_c \tau_k(t)} \delta(t - \tau_k(t)). \quad (19)$$

Here  $\alpha_k(t)$  is the complex path weight,  $\tau_k(t)$  is the time-variant propagation delay, and  $f_c$  is the carrier frequency.

TABLE I  
COMPARISON OF CORRELATION AND PROBABILITY BASED FUNCTIONS FOR US CHANNELS

Function Name	Bello [6]	Matz [9]	Walter et.al.	Function Name
time-variant local scattering function	–	$C_{\mathbf{H}}(t; \tau, \nu)$	$p(t; \tilde{\tau}, \nu)$	TV joint delay Doppler pdf
TC delay cross-power spectral density	$P_g(t, s; \xi)$	$P_h(t; \tau, \Delta t)$	$\rho(t; \tilde{\tau}, \Delta t)$	TV hybrid time delay char. pdf
–	–	–	$\varrho(t; \Delta \tilde{f}, \nu)$	TV hybrid freq. Doppler char. pdf
autocorrelation of time-variant transfer function	$R_T(\Omega; t, s)$	$R_L(t; \Delta t, \Delta f)$	$r(t; \Delta \tilde{f}, \Delta t)$	TV joint time frequency char. fun.
DC delay cross-power spectral density	$P_U(\xi; \nu, \mu)$	$P_S(\tau, \nu; \Delta \nu)$	$\rho(\Delta \nu; \tilde{\tau}, \nu)$	DV hybrid Doppler delay char. pdf
–	–	–	$\varrho(\Delta \nu; \tilde{\tau}, \Delta t)$	DC hybrid time delay char. pdf
autocorrelation of output Doppler spread function	$R_G(\Omega; \nu, \mu)$	–	$r(\Delta \nu; \Delta \tilde{f}, \nu)$	DV joint freq. Doppler char. fun.
uncorrelated scatter channel correlation function	–	$\mathcal{A}_{\mathbf{H}}(\Delta t, \Delta f; \Delta \nu)$	$\mathcal{R}(\Delta \nu; \Delta \tilde{f}, \Delta t)$	triple freq. Doppler time char. fun.

TV: time-variant, TC: time correlated, DV: Doppler-variant, DC: Doppler correlated

By taking the Fourier transform over the delay, a time-variant transfer function can be constructed as

$$L(t, f) = \sum_{k=0}^{K(t)-1} \alpha_k(t) e^{-j2\pi(f+f_c)\tau_k(t)}. \quad (20)$$

We approximate the time-variant channel with a piece-wise linear approximation. This is done by assuming that for a moment of time  $t = t'$  the time-variant path propagation delay can be locally, over the interval  $\Delta t$ , approximated with a MacLauren series. Thus, we can represent a time-variant delay as

$$\tau_k(t) = \sum_{n=0}^{\infty} \frac{1}{n!} \left. \frac{d\tau_k(t)}{dt} \right|_{t=t'} t^n \approx \bar{\tau}_k(t') + t \left. \frac{d\tau_k(t)}{dt} \right|_{t=t'}. \quad (21)$$

Note that in general,  $\bar{\tau}_k(t')$  is constant over the assumed interval  $\Delta t$ . The derivative  $\left. \frac{d\tau_k(t)}{dt} \right|_{t=t'}$  is also constant over this interval. These parameters characterize the intercept and local linear trend of the time-variant delay  $\tau_k(t)$  at a point  $t'$ . They do, however, change with time  $t$ , yet at a lower rate. In other words, they are piece-wise constant functions of  $t$ . In the following, we will make the dependency of these variables on  $t$  explicit, keeping the piece-wise constant nature of these variables in mind.

We note that under the narrow-band assumption, the Doppler frequency  $\nu(t)$  can be defined as  $\nu(t) \triangleq -f_c \frac{d\tau(t)}{dt}$ , i.e., when all transmitted frequencies experience the same Doppler shift [13]. Using (21) the time-variant transfer function  $L(t, f)$  can be approximated as

$$L(t, f) \approx \sum_{k=0}^{K(t)-1} \check{\alpha}_k(t) e^{j2\pi\nu_k(t)t} e^{-j2\pi f \bar{\tau}_k(t)}, \quad (22)$$

where  $\check{\alpha}_k(t) = \alpha_k(t) e^{-j2\pi f_c \bar{\tau}_k(t)}$ . For the correlation function, we get with  $\tilde{\tau} = \tau/\tau_{\text{los}}$  and  $\tilde{f} = f/\tau_{\text{los}}$  as shown in [11] and [13] the following

$$R_L(t; \Delta t, \Delta \tilde{f}) = |\check{\alpha}(t)|^2 \mathbb{E} \left\{ e^{j2\pi\nu_k(t)\Delta t} e^{-j2\pi\Delta \tilde{f} \bar{\tau}_k(t)} \right\}, \quad (23)$$

where the expectation  $\mathbb{E}\{\cdot\}$  is taken with respect to the joint distribution  $p(t; \tilde{\tau}, \nu)$ . The result of  $\mathbb{E}\{\cdot\}$  in (23) is the joint characteristic function  $r(t; \Delta \tilde{f}, \Delta t)$  as given in (12). Thus, the correlation function  $R_L$  is proportional to the joint

characteristic function  $r(t; \Delta \tilde{f}, \Delta t)$ . This relationship between correlation function and characteristic function is similarly shown in [23] if complex exponentials are used for the channel representation. Let us stress again that the proportionality is valid for an arbitrary, but fixed  $t = t'$  and as  $\Delta t \rightarrow 0$ .  $\square$

Following directly from Theorem 1, we can derive the ensuing proportionality relations due to the linearity of the Fourier transform of the time-variant, two-dimensional correlation based and probability based functions. They are given for the four time-variant functions by

$$\begin{aligned} R_L(t; \Delta t, \Delta \tilde{f}) &\propto r(t; \Delta \tilde{f}, \Delta t), \\ C_{\mathbf{H}}(t; \tilde{\tau}, \nu) &\propto p(t; \tilde{\tau}, \nu) \\ P_h(t; \tilde{\tau}, \Delta t) &\propto \rho(t; \tilde{\tau}, \Delta t), \\ P_\varrho(t; \Delta \tilde{f}, \nu) &\propto \varrho(t; \Delta \tilde{f}, \nu). \end{aligned} \quad (24)$$

Furthermore, this allows us to define the following conditional descriptions for the correlation based functions, which are then equal to the conditional probability based functions as

$$\begin{aligned} C_{\mathbf{H}}(t; \nu | \tilde{\tau}) &\triangleq \frac{C_{\mathbf{H}}(t; \tilde{\tau}, \nu)}{P_h(t; \tilde{\tau}, \Delta t = 0)} = p(t; \nu | \tilde{\tau}), \\ P_h(t; \Delta t | \tilde{\tau}) &\triangleq \frac{P_h(t; \tilde{\tau}, \Delta t)}{P_h(t; \tilde{\tau}, \Delta t = 0)} = \rho(t; \Delta t | \tilde{\tau}), \\ P_\varrho(t; \Delta \tilde{f} | \nu) &\triangleq \frac{P_\varrho(t; \Delta \tilde{f}, \nu)}{P_\varrho(t; \Delta \tilde{f} = 0, \nu)} = \varrho(t; \Delta \tilde{f} | \nu), \end{aligned} \quad (25)$$

where we use the fact that computing the hybrid characteristic function at zero lag is equivalent to the marginalization of the pdf. Similar to [24], we can compute the normalized power spectral densities and correlation functions, which are again equal to their probability based counterparts as

$$\begin{aligned} \tilde{P}_h(t; \tilde{\tau}) &= \frac{P_h(t; \tilde{\tau}, \Delta t = 0)}{\int P_h(t; \tilde{\tau}, \Delta t = 0) d\tilde{\tau}} = p(t; \tilde{\tau}), \\ \tilde{P}_\varrho(t; \nu) &= \frac{P_\varrho(t; \Delta \tilde{f} = 0, \nu)}{\int P_\varrho(t; \Delta \tilde{f} = 0, \nu) d\nu} = p(t; \nu), \\ \tilde{R}_L(t; \Delta \tilde{f}, \Delta t) &= \frac{R_L(t; \Delta t, \Delta \tilde{f})}{R_L(t; \Delta t = 0, \Delta \tilde{f} = 0)} = r(t; \Delta \tilde{f}, \Delta t), \\ \tilde{R}_L(t; \Delta \tilde{f}) &= \frac{R_L(t; \Delta t = 0, \Delta \tilde{f})}{R_L(t; \Delta t = 0, \Delta \tilde{f} = 0)} = r(t; \Delta \tilde{f}), \\ \tilde{R}_L(t; \Delta t) &= \frac{R_L(t; \Delta t, \Delta \tilde{f} = 0)}{R_L(t; \Delta t = 0, \Delta \tilde{f} = 0)} = r(t; \Delta t). \end{aligned} \quad (26)$$

Thus, a direct comparison between the correlation based and the probability based functions becomes possible.

### III. HYBRID CHARACTERISTIC PDF

In order to obtain an analytical closed-form solution for the hybrid time delay characteristic pdf, we have to transform the spatial coordinates into an adequate coordinate system. We have shown in [25] that a prolate spheroidal coordinate system is suitable for this purpose. The prolate spheroidal coordinate system (PSCS) allows for a delay-dependent description of the M2M channel by exploiting the symmetry of the channel by an ellipsoid based delay description. We shortly summarize the corresponding formal steps to obtain the spatial distribution of scatterers from [20] and introduce the coordinate system.

#### A. Prolate Spheroidal Coordinates

The transformation between the Cartesian coordinate system (CCS)  $(x, y, z)$  and the prolate spheroidal coordinates (PSCs)  $(\xi, \eta, \vartheta)$  is given by the following equations

$$\begin{aligned} x &= l\sqrt{(\xi^2 - 1)(1 - \eta^2)} \cos \vartheta, \\ y &= l\sqrt{(\xi^2 - 1)(1 - \eta^2)} \sin \vartheta, \\ z &= l\xi\eta, \end{aligned} \quad (27)$$

where  $\xi \in [1, \infty)$ ,  $\eta \in [-1, 1]$ ,  $\vartheta \in [0, 2\pi)$  are the new coordinates and  $l$  in (27) is the focus distance of both TX and RX to the origin of the Cartesian and the prolate spheroidal coordinate system. The coordinate  $\xi$  represents the constant distance between TX and RX via a single-bounce reflection. Geometrically, this relationship is represented by an ellipsoid, as shown in Fig. 3. We can also define a delay based coordinate system. This is given by

$$\begin{aligned} \tau_x &= \frac{\tau_{1os}}{2} \sqrt{(\tilde{\tau}^2 - 1)(1 - \eta^2)} \cos \vartheta, \\ \tau_y &= \frac{\tau_{1os}}{2} \sqrt{(\tilde{\tau}^2 - 1)(1 - \eta^2)} \sin \vartheta, \\ \tau_z &= \frac{\tau_{1os}}{2} \tilde{\tau}\eta, \end{aligned} \quad (28)$$

which has temporal axes in units of seconds. Note that the variable that determines the size of the ellipsoid is denoted by  $\xi$ . However, since  $2l = c\tau_{1os}$  with  $c$  being the speed of light, it follows that  $\xi \equiv \tilde{\tau}$ . Furthermore, the classical delay from channel modeling is given as  $\tau = \tau_{1os}\tilde{\tau}$ .

Let us consider a scattering plane via which a signal propagates to the receiver. An arbitrarily oriented scattering plane is given in Cartesian coordinates as

$$Ax + By + Cz = lD, \quad (29)$$

where the four parameters  $\{A, B, C, D\} \in \mathbb{R}$  determine its orientation in space. For our purposes we express (29) in the PSCs, from (27) which results in

$$\begin{aligned} Al\sqrt{(\xi^2 - 1)(1 - \eta^2)} \cos \vartheta + Bl\sqrt{(\xi^2 - 1)(1 - \eta^2)} \sin \vartheta \\ + Cl\xi\eta = lD. \end{aligned} \quad (30)$$

The scattering plane, as any 2D plane embedded in 3D space, can be parameterized by two independent variables

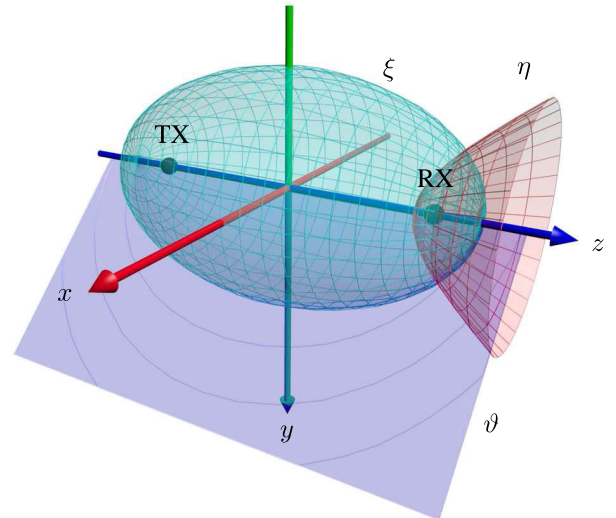


Fig. 3. Prolate spheroidal coordinate system with the surfaces of constant  $\xi$  (ellipsoid),  $\eta$  (hyperboloid), and  $\vartheta$  (half-plane) with the TX and RX in the foci of the ellipsoid and hyperboloid.

in the selected coordinate system. Our goal is to obtain a parameterization that allows for a closed-form derivation of the hybrid time delay characteristic pdf. Since we already have  $\xi$  for a distance-dependent description, we can choose either  $\eta$  or  $\vartheta$  as the second variable. In fact, we need both the  $(\xi, \eta)$  and  $(\xi, \vartheta)$  parameterizations to cover all possible scattering planes in 3D space. Our main parameterization, however, is in  $(\xi, \eta)$ -coordinates. The remaining scattering planes, which cannot be parameterized by  $(\xi, \eta)$ , since they are orthogonal to the  $z$ -axis in the local CCS, are described by the  $(\xi, \vartheta)$ -coordinates. The  $(\xi, \vartheta)$  description actually complements the  $(\xi, \eta)$  parameterization. In the following, we refer to these cases as *general case* and *complementary case*, respectively.

#### B. Spatial Probability Density

In order to obtain the spatial distribution of the scatterers we restrict our analysis to scatterers lying on the scattering plane. We consider scatterers that lie on the portion of the scattering plane circumscribed by the intersection ellipse. The resulting scattering ellipse can be generally described by the implicit expression  $q(\xi, \eta, \vartheta) = 0$ , which simplifies to  $q(\xi, \eta) = 0$ , if the parameterization is in  $(\xi, \eta)$ -coordinates or  $q(\xi, \vartheta) = 0$ , if the parameterization is in  $(\xi, \vartheta)$ -coordinates. We assume that the scatterers lying within  $q(\xi, \eta, \vartheta) = 0$  are identical and uniformly distributed. Thus, the two-dimensional density  $\mathbf{s}$  of the scatterers within the scattering ellipse is modeled as

$$p(t, q(\xi, \eta, \vartheta); \mathbf{s}) = \frac{1}{\mathcal{Y}}, \quad (31)$$

where  $\mathcal{Y}$  is the equivalent area of the ellipse  $q(\xi, \eta, \vartheta) = 0$ .

The joint delay Doppler pdf is then obtained by transforming the distribution of scatterers  $\mathbf{s}$  into  $(\xi, \nu)$ -coordinates using (49) and rules of probability transformation as

$$p(t, q(\xi, \eta, \vartheta); \xi, \nu) = p(t, q(\xi, \eta, \vartheta); \mathbf{s}) \left| \mathbf{J}_{\mathbf{s}}^{-1} \right|, \quad (32)$$

where  $\mathbf{J}_s^{-1}$  is the inverse  $2 \times 2$  Jacobian matrix of the variable transformation.

For the joint delay Doppler pdf, the transformation from the spatial domain to the Doppler domain, i.e.,  $s \mapsto \nu$  or  $s \mapsto (\xi, \nu)$  introduces ambiguities in the mapping. These ambiguities, however, can be resolved by applying the algebraic curve theory to the Doppler frequency description, see [20]. Furthermore, the locations of the extrema and thus the limiting frequencies of the pdfs can be determined.

Subsequently, we have to determine the scattering areas of surfaces in curvilinear coordinates in order to normalize the spatial pdfs. To this end, we employ the concept of differential forms, which are shortly explained hereafter.

According to [26] a differential form is similar to an integrand. With differential forms the differential operators like gradient, divergence, and rotation are extended to higher dimensions. In PSCs, we apply differential forms [27] to derive the integrands, i.e., the differential area in PSCs which is required to normalize the pdfs in (31). We determine the normalization constant of the spatial pdf by using differential 2-forms.

In order to calculate the area in PSCs, we have to convert the differentials of the coordinates from the local CCS to the PSCs. The differentials are transformed by using the Jacobian matrix  $\mathbf{J}$  according to [28] as

$$\begin{aligned} [dx, dy, dz]^T &= \mathbf{J}[d\xi, d\eta, d\vartheta]^T, \\ \begin{pmatrix} dx \\ dy \\ dz \end{pmatrix} &= \begin{pmatrix} \frac{\partial x}{\partial \xi} & \frac{\partial x}{\partial \eta} & \frac{\partial x}{\partial \vartheta} \\ \frac{\partial y}{\partial \xi} & \frac{\partial y}{\partial \eta} & \frac{\partial y}{\partial \vartheta} \\ \frac{\partial z}{\partial \xi} & \frac{\partial z}{\partial \eta} & \frac{\partial z}{\partial \vartheta} \end{pmatrix} \begin{pmatrix} d\xi \\ d\eta \\ d\vartheta \end{pmatrix}. \end{aligned} \quad (33)$$

The differential area  $dS$  of an arbitrarily oriented scattering plane as a nonlinear 2-form is given by [26] as

$$dS = \sqrt{(dx \wedge dy)^2 + (dy \wedge dz)^2 + (dz \wedge dx)^2}, \quad (34)$$

where  $\wedge$  is the wedge product used as

$$\beta \wedge \gamma = (-1)^{kp} \gamma \wedge \beta, \quad (35)$$

with  $\beta$  being a  $k$ -form and  $\gamma$  an  $p$ -form. The wedge product is alternating by construction meaning  $dx \wedge dy = -dy \wedge dx$  and  $dx \wedge dx = 0$  for two differential 1-forms. The complete area of a scattering plane is computed according to [26] as

$$S = \int_{\mathcal{S}} g(x, y, z) \sqrt{(dx \wedge dy)^2 + (dy \wedge dz)^2 + (dz \wedge dx)^2}, \quad (36)$$

where the integral determines the scattering area of a graph  $g(x, y, z)$  over the surface  $\mathcal{S} := q(\xi, \eta, \vartheta) = 0$ . The region is bounded by  $\xi = \xi_{\max}$  corresponding to the maximum normalized distance that the user can set arbitrarily.

For the scattering plane  $q(\xi, \eta, \vartheta)$ , the area calculation in (36) is calculated using three different equations as

$$S = \begin{cases} \int_{\mathcal{S}} \sqrt{\left(\frac{\partial g_1}{\partial x}\right)^2 + \left(\frac{\partial g_1}{\partial y}\right)^2 + 1} |dx \wedge dy| & \text{if } C \neq 0, \\ \int_{\mathcal{S}} \sqrt{\left(\frac{\partial g_2}{\partial y}\right)^2 + \left(\frac{\partial g_2}{\partial z}\right)^2 + 1} |dy \wedge dz| & \text{if } A \neq 0, \\ \int_{\mathcal{S}} \sqrt{\left(\frac{\partial g_3}{\partial z}\right)^2 + \left(\frac{\partial g_3}{\partial x}\right)^2 + 1} |dz \wedge dx| & \text{if } B \neq 0, \end{cases} \quad (37)$$

depending on the parametrization of the scattering plane in (29). The plane is implicitly parametrized by  $z = g_1(x, y)$ ,  $x = g_2(y, z)$  or  $y = g_3(z, x)$ . In the following, the three square roots are referred to as  $r_i$  and the differential areas  $dS_i$  are special cases of (34). At the end we determine the weighted area  $\mathcal{Y}$  of the intersection for computing the joint delay Doppler pdf in (31) as

$$\mathcal{Y} = \int_{\mathcal{S}} w r_i dS_i, \quad (38)$$

where  $r_i$ ,  $i \in \{1, 2, 3\}$ , is the square root in (37). We select it according to the chosen parameterization of the scattering plane  $g_i$ . The differential area  $dS_i$  is either given by  $|dx \wedge dy|$  or  $|dy \wedge dz|$  or  $|dz \wedge dx|$  depending on the scattering plane parameterization. The path loss inspired weighting function is given by  $w$ .

Again, we differentiate the *general case* and the *complementary case*. The former can be calculated from the last two lines in (37), while the latter is computed with the first line in (37) using  $A = B = 0$ .

After substituting the wedge products of the Cartesian differentials with the differentials in PSCs according to (33), the area of the scattering ellipse is computed in PSCs. For the *general case* the differential area of an arbitrary plane is given by

$$r_i dS_i = \frac{l^2 \sqrt{A^2 + B^2 + C^2} (\xi^2 - \eta^2)}{\sqrt{(\xi^2 - 1)(1 - \eta^2)(A^2 + B^2) - (D - C\xi\eta)^2}} d\eta d\xi \quad (39)$$

where  $i \in \{1, 2, 3\}$  relates to the three integrals in (37). The term  $r_i dS_i$  provides the differential area in order to compute the total area of the ellipse defined by the distance ellipsoid and the scattering plane. Note that the wedge product is replaced by a normal product, since the limits of the integrals together with the integrand produce a positive area.

For the *complementary case* the differential area of a scattering plane orthogonal to the  $z$ -axis in PSCs is given by

$$r_1 dS_1 = l^2 \left( \xi - \frac{D^2}{C^2 \xi^3} \right) d\vartheta d\xi, \quad (40)$$

which relates to the first line in (37) with  $A = B = 0$  and thus  $r_1 = 1$ . The integral over the differential area computes the area of a circle, which is caused by intersecting the scattering plane and the distance ellipsoid, since the scattering plane is orthogonal to the  $z$ -axis.

In order to use a spatial distribution of the scatterers, we need to calculate the area enclosed by the delay ellipsoid. Additionally, we need a weighting function  $w(\xi, \eta)$  that takes into account the path loss, which follows from the radar equation [29] as

$$w(\xi, \eta) = \frac{1}{(\xi^2 - \eta^2)^2}. \quad (41)$$

This essentially states that the received power is proportional to the squared distances from the scatterer to TX and RX as  $P \propto (d_t^2 d_r^2)^{-1}$ .

For the *general case*, we obtain the following equation for the weighted elliptic area

$$\begin{aligned} \mathcal{Y}_1 &= \int_{\xi_{\min}}^{\xi_{\max}} 2 \int_{\eta_1(\xi)}^{\eta_2(\xi)} \frac{w(\xi, \eta) l^2 \sqrt{A^2 + B^2 + C^2} (\xi^2 - \eta^2) d\eta d\xi}{\sqrt{(\xi^2 - 1)(1 - \eta^2)(A^2 + B^2) - (D - C\xi\eta)^2}}, \end{aligned} \quad (42)$$

where  $\xi_{\max} > \xi_{\min} > \xi_{\text{sr}}$  is the minimum and maximum normalized distance, which can be set by the user and  $\xi_{\text{sr}} \equiv \tilde{\tau}_{\text{sr}}$  according to (15). The other parameters  $\eta_2(\xi) > \eta_1(\xi)$  are given by (51), shown at the bottom of the next page.

For the *complementary case* we obtain a weighted circular area as a special case of the elliptic area, since the semi-major axis of the delay ellipsoid is orthogonal to the scattering plane. It is given by

$$\begin{aligned} \mathcal{Y}_2 &= \int_{q(\xi, \eta, \vartheta)=0} \int w\left(\xi, \frac{D}{C\xi}\right) dS_1 \\ &= \int_{\xi_{\min}}^{\xi_{\max}} \int_0^{2\pi} \frac{l^2 \left(\xi - \frac{D^2}{C^2\xi^3}\right)}{\left(\xi^2 - \left(\frac{D}{C\xi}\right)^2\right)^2} d\vartheta d\xi, \end{aligned} \quad (43)$$

where  $dS_1 = d\vartheta d\xi$  is the differential scattering area with  $\xi_{\max} > \xi_{\min} > \xi_{\text{sr}}$  defined similarly to the *general case*.

For deriving the hybrid time delay characteristic pdf, we use the spatial density of the scatterers instead of transforming the Doppler frequency  $\nu$ , as was done in previous works, e.g., [11] and [30] for the delay-dependent description. We thus either transform over the variable  $\eta$  for the *general case* or over the variable  $\vartheta$  for the *complementary case*.

Note that we do not provide the derivation with the simpler delay-dependent description based on the length of the intersection as in previous publications. Thus, we present the more realistic case of the area of the intersection ellipse, where the differential scatterers have a two-dimensional displacement.

### C. Hybrid Time Delay Characteristic Probability Density

In this subsection, we first derive the hybrid characteristic pdf  $\rho(t; \xi, \Delta t)$  in normalized distance  $\xi$  and time lag  $\Delta t$  domains for general M2M scattering channels. Then we show it is equal to the hybrid characteristic pdf  $\rho(t; \tilde{\tau}, \Delta t)$  in normalized delay  $\tilde{\tau}$  and time lag  $\Delta t$  as discussed in Section II. Since our starting point is the joint delay Doppler pdf, we obtain

the hybrid characteristic probability density function by an inverse Fourier transform in the Doppler frequency variable. We show that in the limiting case, those newly derived hybrid characteristic pdfs converge to known results of correlation functions in the literature, e.g. the Bessel function as in [4].

We obtain the hybrid characteristic pdfs for the *general case*, as it was defined above, by using the spatial variable  $\eta$  instead of the Doppler frequency  $\nu$ . By using relationship (32), we obtain by using (52), shown at the bottom of the next page.

$$\begin{aligned} \rho(t; \xi, \Delta t) &= \sum_{i=1}^2 \int p(t, q(\xi, \eta, \vartheta); \xi, \nu) e^{j2\pi\Delta t\nu_i^*} d\nu_i^* \\ &= \sum_{i=1}^2 \int p(t, q(\xi, \eta, \vartheta); \xi, \nu(\eta)) e^{j2\pi\Delta t\nu_i^*(\eta)} |\mathbf{J}_s| d\eta. \end{aligned} \quad (44)$$

Thus, we can directly insert the differential and weighted spatial scatterer density  $r_i dS_i$  and  $\mathcal{Y}_1$  according to (39) and (42) and perform the inverse Fourier function over  $\eta$  as

$$\begin{aligned} \rho(t; \xi, \Delta t) &= \frac{1}{\mathcal{Y}_1} \sum_{i=1}^2 \int_{\eta_1(\xi)}^{\eta_2(\xi)} \\ &\quad \times \frac{w(\xi, \eta) l^2 \sqrt{A^2 + B^2 + C^2} (\xi^2 - \eta^2) e^{j2\pi\Delta t\nu_i^*(t; \xi, \eta)}}{\sqrt{(\xi^2 - 1)(1 - \eta^2)(A^2 + B^2) - (D - C\xi\eta)^2}} d\eta, \end{aligned} \quad (45)$$

with the time-variant Doppler frequency  $\nu_i^*(t; \xi, \eta)$  according to (52) and the integral limits  $\eta_1(\xi)$  and  $\eta_2(\xi)$  according to (51) with  $\eta_2(\xi) > \eta_1(\xi)$ .

For the *complementary case* we insert the differential and weighted circular area  $r_1 dS_1$  and  $\mathcal{Y}_2$  given in (40) and (43) and can calculate the hybrid characteristic pdf by an inverse Fourier transform of the Doppler variable  $\nu$  as

$$\begin{aligned} \rho(t; \xi, \Delta t) &= \frac{1}{\mathcal{Y}_2} \int_0^{2\pi} \frac{l^2 \left(\xi - \frac{D^2}{C^2\xi^3}\right)}{\left(\xi^2 - \left(\frac{D}{C\xi}\right)^2\right)^2} e^{j2\pi\nu(t; \xi, \vartheta)\Delta t} d\vartheta \\ &= \frac{2l^2 \left(\xi - \frac{D^2}{C^2\xi^3}\right)}{\mathcal{Y}_2 \left(\xi^2 - \left(\frac{D}{C\xi}\right)^2\right)^2} \int_{-\nu_{\text{lim}}}^{\nu_{\text{lim}}} \frac{e^{j2\pi\nu\Delta t}}{\nu_{\text{lim}} \sqrt{1 - \left(\frac{\nu - \nu_o}{\nu_{\text{lim}}}\right)^2}} d\nu \\ &= \frac{1}{\mathcal{Y}_2} \frac{2\pi l^2 \left(\xi - \frac{D^2}{C^2\xi^3}\right)}{\left(\xi^2 - \left(\frac{D}{C\xi}\right)^2\right)^2} J_0(2\pi\nu_{\text{lim}}(t; \xi)\Delta t) e^{j2\pi\nu_o(t; \xi)\Delta t}, \end{aligned} \quad (46)$$

where  $J_0$  is the zeroth-order Bessel function of the first kind,

$$\nu_o(t; \xi) = \frac{f_c}{c} \left( \frac{\frac{D}{C} + 1}{\xi + \frac{D}{C\xi}} v_{tz} + \frac{\frac{D}{C} - 1}{\xi - \frac{D}{C\xi}} v_{rz} \right), \quad (47)$$

is the offset frequency caused by the movement of TX and RX along the  $z$ -axis, and

$$\begin{aligned} \nu_{\text{lim}}(t; \xi) &= \frac{f_c}{c} \sqrt{(\xi^2 - 1) \left(1 - \left(\frac{D}{C\xi}\right)^2\right)} \\ &\times \sqrt{\left(\frac{v_{tx}}{\xi + \frac{D}{C\xi}} + \frac{v_{rx}}{\xi - \frac{D}{C\xi}}\right)^2 + \left(\frac{v_{ty}}{\xi + \frac{D}{C\xi}} + \frac{v_{ry}}{\xi - \frac{D}{C\xi}}\right)^2}, \end{aligned} \quad (48)$$

is the limiting frequency. The basis for our calculations above is the Doppler frequency in [20, (3)] as

$$\begin{aligned} \nu(t; \xi, \eta, \vartheta) &= \frac{f_c}{c} \\ &\times \left( \frac{\xi\eta + 1}{\xi + \eta} v_{tz} + \frac{\sqrt{(\xi^2 - 1)(1 - \eta^2)}}{\xi + \eta} (v_{tx} \cos \vartheta + v_{ty} \sin \vartheta) \right. \\ &\left. + \frac{\xi\eta - 1}{\xi - \eta} v_{tz} + \frac{\sqrt{(\xi^2 - 1)(1 - \eta^2)}}{\xi - \eta} (v_{rx} \cos \vartheta + v_{ry} \sin \vartheta) \right) \end{aligned} \quad (49)$$

where  $\mathbf{v}_t = [v_{tx}, v_{ty}, v_{tz}]^T$  and  $\mathbf{v}_r = [v_{rx}, v_{ry}, v_{rz}]^T$  are the velocity vectors of TX and RX in the local CCS, respectively. Since we obtain the relationship  $\eta = D/(C\xi)$  for the *complementary case*, the Doppler frequency reduces to  $\nu(t; \xi, \vartheta)$ . Note that in the *complementary case* the delay and Doppler pdfs factor, and thus are independent of each other.

Since in the calculation of (45) and (46) the focus distance  $l^2$  is canceled out by the normalization factor  $\mathcal{Y}_i$ , the hybrid time distance characteristic pdf is unitless. With the relation  $\xi \equiv \tilde{\tau}$ , we can thus infer that the hybrid time delay characteristic pdf is equal to the hybrid time distance characteristic pdf for normalized delays and distances. This is true, because the two coordinate systems in (27) and (28) inherit their physical units from either  $l$  or  $\tau_{\text{los}}$  and not from  $\xi$  or  $\tilde{\tau}$ . We therefore finally obtain the hybrid time delay characteristic pdf by

$$\rho(t; \tilde{\tau}, \Delta t) \equiv \rho(t; \xi, \Delta t). \quad (50)$$

After having derived the hybrid time delay characteristic pdf, we want to investigate in the following subsection the limiting values for the delay-dependent characteristic function and delay-dependent pdf. This is the reason, why we calculate and compare these two functions.

#### D. Limiting Value Consideration

By studying the delay-dependent Doppler pdf and the delay-dependent characteristic function in the asymptotic regime, as  $\tilde{\tau} \rightarrow \infty$ , we obtain several well-known expressions, e.g., the Bessel function and the Jakes spectrum in [4] and [5]. To this end, we derive

$$\lim_{\tilde{\tau} \rightarrow \infty} \rho(t; \Delta t | \tilde{\tau}) = J_0 \left( 2\pi \Delta t \frac{\|\mathbf{v}_{t\parallel\mathbf{E}} + \mathbf{v}_{r\parallel\mathbf{E}}\|}{c} f_c \right), \quad (53)$$

$$\lim_{\tilde{\tau} \rightarrow \infty} p(t; \nu | \tilde{\tau}) = \frac{1}{\pi \nu_{\text{lim}\infty}(t) \sqrt{1 - \left(\frac{\nu}{\nu_{\text{lim}\infty}(t)}\right)^2}}, \quad (54)$$

$$\lim_{\tilde{\tau} \rightarrow \infty} \mu_{\nu | \tilde{\tau}}(t; \nu) = 0, \quad (55)$$

$$\lim_{\tilde{\tau} \rightarrow \infty} \sigma_{\nu | \tilde{\tau}}(t; \nu) = \frac{\|\mathbf{v}_{t\parallel\mathbf{E}} + \mathbf{v}_{r\parallel\mathbf{E}}\|}{\sqrt{2}c} f_c = \frac{\nu_{\text{lim}\infty}(t)}{\sqrt{2}}, \quad (56)$$

with the zeroth-order Bessel function  $J_0$ . The parallel velocity vectors and limiting Doppler frequency given by

$$\mathbf{v}_{t\parallel\mathbf{E}} = \frac{\mathbf{n}_E \times (\mathbf{v}_t \times \mathbf{n}_E)}{\|\mathbf{n}_E\|^2} = \mathbf{v}_t - \frac{(\mathbf{v}_t \cdot \mathbf{n}_E) \mathbf{n}_E}{\|\mathbf{n}_E\|^2}, \quad (57)$$

$$\mathbf{v}_{r\parallel\mathbf{E}} = \frac{\mathbf{n}_E \times (\mathbf{v}_r \times \mathbf{n}_E)}{\|\mathbf{n}_E\|^2} = \mathbf{v}_r - \frac{(\mathbf{v}_r \cdot \mathbf{n}_E) \mathbf{n}_E}{\|\mathbf{n}_E\|^2}, \quad (58)$$

$$\lim_{\tilde{\tau} \rightarrow \infty} \nu_{\text{lim}\infty}(t) = \frac{\|\mathbf{v}_{t\parallel\mathbf{E}} + \mathbf{v}_{r\parallel\mathbf{E}}\|}{c} f_c. \quad (59)$$

The velocity vectors  $\mathbf{v}_{t\parallel\mathbf{E}}$  in (57) and  $\mathbf{v}_{r\parallel\mathbf{E}}$  in (58) of TX and RX are parallel to the scattering plane and  $\mathbf{n}_E = [A, B, C]^T$  is the normal vector of the scattering plane. The limiting frequency  $\nu_{\text{lim}\infty}(t)$  in (59) for  $\tilde{\tau} \rightarrow \infty$  is given by the solution of the  $\eta$  variable  $\pm (v_{tz\parallel\mathbf{E}} + v_{rz\parallel\mathbf{E}}) / (\|\mathbf{v}_{t\parallel\mathbf{E}} + \mathbf{v}_{r\parallel\mathbf{E}}\|)$  of the polynomial in [20, (31)]. The result in (54) matches the classical Jakes result in [5]. The width of the spectrum, however, is determined by the velocity vector components of TX and

---


$$\eta_{1,2}(\xi) = \frac{DC\xi \pm \sqrt{D^2C^2\xi^2 - (A^2\xi^2 + B^2\xi^2 + C^2\xi^2 - A^2 - B^2)(A^2 + B^2 + D^2 - A^2\xi^2 - B^2\xi^2)}}{A^2\xi^2 + B^2\xi^2 + C^2\xi^2 - A^2 - B^2} \quad (51)$$


---

$$\begin{aligned} \nu_i^*(t; \xi, \eta) &= \frac{1}{(A^2 + B^2)(\xi^2 - \eta^2)} \left( (D - C\xi\eta) (A(v_{rx}(\xi + \eta) + v_{tx}(\xi - \eta)) + B(v_{ry}(\xi + \eta) + v_{ty}(\xi - \eta))) \right. \\ &\pm \sqrt{\left( (\xi^2 - 1)(1 - \eta^2)(A^2 + B^2) - (D - C\xi\eta)^2 \right) (B(v_{rx}(\xi + \eta) + v_{tx}(\xi - \eta)) - A(v_{ry}(\xi + \eta) + v_{ty}(\xi - \eta)))^2} \\ &\left. + (A^2 + B^2) (v_{rz}(\xi\eta - 1)(\xi + \eta) + v_{tz}(\xi\eta + 1)(\xi - \eta)) \right) \frac{f_c}{c} \end{aligned} \quad (52)$$

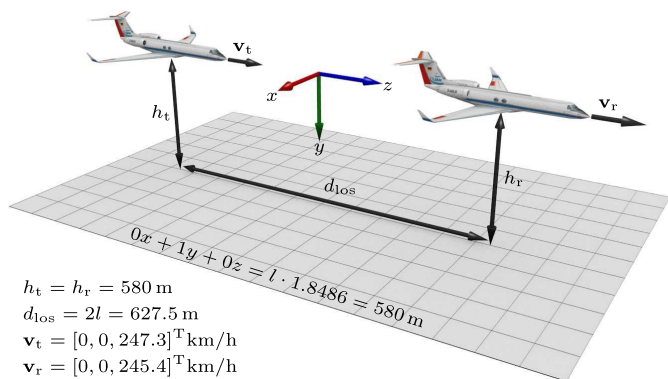


Fig. 4. Aircraft positions, velocity vectors, distance and placement of the scattering plane in a local coordinate system for simulation.

RX, which are parallel to the scattering plane. The reason for this is that for large  $\tilde{\tau}$  the eccentricity of the ellipsoid reduces toward 0, thus approaching a sphere. The intersection with the scattering plane hence results in a scattering circle on which the scatterers are uniformly distributed. The corresponding Fourier transform of the delay-dependent pdf in (54) results in the typical Bessel function in (53) shown in [4] as the delay-dependent characteristic function  $\rho(t; \Delta t | \tilde{\tau})$ .

#### IV. COMPARATIVE ANALYSIS OF THEORY AND MEASUREMENT

In our previous works [20] and [30], we primarily examined the scattering contributions in terms of delay and Doppler frequency shift. However, the decrease in the scattering power with increasing delay, reflecting the influence of the channel's power delay profile (PDP), has not yet been addressed and verified. The typical approach to account for the PDP is to empirically adjust the scattering power behavior using a specific path loss exponent, e.g., as in [22]. In contrast to these empirical approaches, the analytical description of the hybrid characteristic pdf of the channel, as presented in this work, allows the calculation of the time-variant PDP for any scenario, taking into account the geometry of the environment and the velocities of the transceivers.

In the following, we examine the aircraft-to-aircraft (A2A) channel as a representative example of a US M2M channel, being the most general channel where both TX and RX are not confined to the scattering plane. We compare data obtained from a measurement campaign [31] and the data obtained from the numerical evaluation of the hybrid characteristic pdf from (45) in Section III.

##### A. Measurement and Simulation Scenario

For the calculation of the corresponding theoretical data, we use the exact same setting from the measurement campaign. These parameters are only dependent on the geometry of the scenario. We consider a scenario in which two aircraft are flying at the same altitude above the ground. The trailing aircraft is at a distance of  $d_{\text{los}} = \tau_{\text{los}}c = 627.5$  m behind the leading aircraft, which corresponds to a line-of-sight propagation delay of  $\tau_{\text{los}} = 2.092 \mu\text{s}$ . With an absolute altitude of  $h_t = h_r = 580$  m above ground and a focus distance of

TABLE II  
MEASUREMENT AND EVALUATION PARAMETERS

Parameter Name	Variable	Value	
Carrier frequency	$f_c$	250 MHz	
Bandwidth	$B$	20 MHz	
Measurement time grid	$\Delta t$	2.048 ms	
Number of carrier	$N_C$	513	
Block length	$N_B$	1023	
Parameter Name	Variable	Relation	Value
Frequency resolution	$\Delta f$	$= B/N_C$	39.1 kHz
Norm. max. frequency	$\tilde{f}_{\text{max}}$	$= \pm B\tau_{\text{los}}/2$	$\pm 20.92$
Norm. frequency resolution	$\Delta \tilde{f}$	$= \Delta f\tau_{\text{los}}$	0.082
Signal period	$\tau_{\text{max}}$	$= 1/\Delta f$	25.6 $\mu\text{s}$
Delay resolution	$\Delta \tau$	$= 1/B$	50 ns
Norm. signal period	$\tilde{\tau}_{\text{max}}$	$= \tau_{\text{max}}/\tau_{\text{los}}$	12.24
Norm. delay resolution	$\Delta \tilde{\tau}$	$= \Delta \tau/\tau_{\text{los}}$	0.024
Time period	$t_{\text{max}}$	$= N_B \Delta t$	2.1 s
Max. Doppler frequency	$\nu_{\text{max}}$	$= \pm 1/(2\Delta t)$	$\pm 244$ Hz
Doppler resolution	$\Delta \nu$	$= 1/t_{\text{max}}$	0.5 Hz

$l = d_{\text{los}}/2 = 313.75$  m, the equation for the scattering plane (29) becomes  $y = 580$  m, meaning the four coefficients are  $A = 0$ ,  $B = 1$ ,  $C = 0$ , and  $D = 1.8486$ . The velocity vectors of both TX and RX are given by  $\mathbf{v}_t = [0, 0, 247.3]^T$  km/h and  $\mathbf{v}_r = [0, 0, 245.4]^T$  km/h. An overview of the scenario including positions of the aircraft, velocity vectors  $\mathbf{v}_t$  and  $\mathbf{v}_r$  in a local CCS, and the parameters of the scattering plane for the simulation is shown in Fig. 4.

The measurement parameters that are given by the channel sounding equipment are provided in Table II. The detailed measurement description, the flight routes, and pictures can be found in [31]. We repeat the most important measurement parameters in the following. The channel sounder generates a periodic, crest factor optimized multitone signal [32], which was transmitted on the TX aircraft with an effective radiated power of 10 W at a carrier frequency of  $f_c = 250$  MHz. The transmitted signal, comprising  $N_C = 513$  carriers, was set to a bandwidth of  $B = 20$  MHz, which results in a frequency resolution of  $\Delta f = 39.1$  kHz. On the RX aircraft, the received signal was recorded every  $\Delta t = 2.048$  ms. Further, we combine  $N_B = 1023$  successively received signals into one block. Based on this setting, we can derive all relevant measurement and evaluation parameters, which are comprehensively summarized in Table II.

The time-variant channel transfer function is thus sampled at discrete frequencies and discrete times and can be written as  $\hat{L}(i\Delta t, n\Delta f)$  with discrete indices  $i = 0, \dots, (N_B - 1)$  and  $n = -(N_C - 1)/2, \dots, (N_C - 1)/2$ . It is calculated as a cross-spectrum between the received data  $Y(i\Delta t, n\Delta f)$  and the calibration data  $C(n\Delta f)$  according to [33] as

$$\hat{L}(i\Delta t, n\Delta f) = \frac{Y(i\Delta t, n\Delta f)C^*(n\Delta f)}{|C(n\Delta f)|^2} = \frac{Y(i\Delta t, n\Delta f)}{C(n\Delta f)}. \quad (60)$$

By applying (inverse) discrete Fourier transforms (DFTs) on  $\hat{L}(i\Delta t, n\Delta f)$ , we obtain the estimated time-variant impulse

response  $\hat{h}(i\Delta t, k\Delta\tau)$  with  $k = 0, \dots, N_B - 1$  and the estimated Doppler-variant transfer function  $\hat{T}(j\Delta\nu, n\Delta f)$  with  $j = -(N_B - 1)/2, \dots, (N_B - 1)/2$ . From  $\hat{h}(i\Delta t, k\Delta\tau)$  and  $\hat{T}(j\Delta\nu, n\Delta f)$ , we can determine the estimated time-variant correlation functions  $P_h(t; \tau, \Delta t)$  and  $R_L(t; \Delta t, \Delta f)$  using (2) and (3). The remaining two time-variant correlation based functions  $\mathcal{C}_H(t; \tau, \nu)$  from (4) and  $P_\varrho(t; \Delta f, \nu)$  from (6) can be calculated indirectly by DFTs.

Using the parameters of the measurement campaign, see Fig. 4 and Table II, we can now calculate the theoretical hybrid characteristic pdf  $\rho(t; \tilde{\tau}, \Delta t)$  with equations (45) and (50). Furthermore, we calculate the joint delay Doppler pdf  $p(t; \tilde{\tau}, \nu)$  using the closed-form solution provided in [20]. Similar to the correlation based function, the remaining two probability based functions  $\varrho(t; \Delta \tilde{f}, \nu)$  and  $r(t; \Delta \tilde{f}, \Delta t)$  are calculated by (inverse) Fourier transform.

### B. Validation Metrics

We evaluate the match of the theory and measurement with the normalized mean squared error (NMSE) and the Pearson correlation coefficient (PCC). The NMSE quantifies the absolute difference in values and therefore provides a measure of how well the measurement matches the model in terms of both magnitude and scale. The PCC measures the linear relationship between the measurement and the model and thus quantifies how strongly variations in the measurement are related to variations in the model. In contrast to the NMSE, the Pearson correlation coefficient indicates, how much the measurement and the model follow the same pattern instead of the how close the values are.

The equation for the NMSE is given by [34]

$$\text{NMSE} = \frac{\sum_{i,k} (P_h(t; \Delta t_i | \tilde{\tau}_k) - \rho(t; \Delta t_i | \tilde{\tau}_k))^2}{\sigma_{P_h}^2}, \quad (61)$$

and the PCC is defined according to [23] as

$$\text{PCC} = \frac{\sum_{i,k} (\rho(t; \Delta t_i | \tilde{\tau}_k) - \mu_\rho) (P_h(t; \Delta t_i | \tilde{\tau}_k) - \mu_{P_h})}{\sigma_\rho \sigma_{P_h}}, \quad (62)$$

where  $\mu_\rho$  and  $\mu_{P_h}$  is the mean and  $\sigma_\rho$  and  $\sigma_{P_h}$  is the standard deviation of  $\rho(t; \Delta t_i | \tilde{\tau}_k)$  and  $P_h(t; \Delta t_i | \tilde{\tau}_k)$ , respectively. The values of the NMSE are  $\geq 0$ , where 0 indicates a perfect match and values  $< 1$  indicate an error smaller than the variance of the data. The values of the PCC are in the range of  $-1$  and  $1$ , where a value of  $1$  indicates perfect linear correlation.

In order to show the advantages of the probability based channel description functions with respect to real world measurements and the corresponding correlation functions, we first compare the conditional and normalized versions of both probability based and correlation based functions. In a second step, we use the non-normalized probabilistic 2D functions and marginalize them to obtain the delay and Doppler spectra and the correlation in the time and frequency domain. We discuss the 2D functions in the same order as in Section II-B.

### C. Equality of Probability and Correlation Based Functions

In this section we compare the conditional probability and correlation functions according to (25). Additionally, we validate the 2D normalized correlation  $\hat{R}_L(t; \Delta \tilde{f}, \Delta t)$  and joint characteristic function  $r(t; \Delta \tilde{f}, \Delta t)$  according to (26). We begin by examining the factorized pdf  $p(t; \nu | \tilde{\tau}) = p(t; \tilde{\tau}, \nu) / p(t; \tilde{\tau})$  in Fig. 5 and compare it with the time-variant, delay-dependent LSF  $\mathcal{C}_H(t; \nu | \tilde{\tau})$  in Fig. 6. Here the joint pdf  $p(t; \tilde{\tau}, \nu)$  can be directly computed from [20] and the time-variant LSF  $\mathcal{C}_H(t; \tilde{\tau}, \nu)$  is obtained by Fourier transform using (4). As Matz predicted in [9] the imaginary and negative parts of the LSF are negligibly small, since we have a doubly underspread channel. Furthermore, we illustrate the delay-dependent mean Doppler  $\mu_{\nu | \tilde{\tau}}(t)$  from (16) and Doppler spread  $\sigma_{\nu | \tilde{\tau}}(t)$  from (17) in Fig. 5. Since the spectra are symmetric, the mean Doppler stays zero, but the Doppler spread is increasing with delay  $\tilde{\tau}$  and approaches, according to (56), the value  $\sigma_{\nu | \tilde{\tau} \rightarrow \infty}(t) = 80.65$  Hz. In the limiting case, the delay-dependent spectrum conforms to a Jakes spectrum according to (54), consistent with the literature. The analysis of the theoretical results in Fig. 5 reveals that the shape and the values of both the probability based and the correlation based functions are the same. The scattering power in the measurement data is very weak and close to the noise threshold. Furthermore, the scattering does not occur uniformly on the ground as in our assumption. Thus, we can observe gaps in Fig. 6. This will lead to slight differences in the marginalized one-dimensional functions. The structure of the measured channel, however, is well captured with the delay-dependent Doppler pdf  $p(t; \nu | \tilde{\tau})$ .

We continue our comparison with the real parts  $\Re$  of the delay-dependent temporal characteristic function  $\rho(t; \Delta t | \tilde{\tau})$  in Fig. 7 and the conditional temporally correlated delay-dependent cross-power density  $P_h(t; \Delta t | \tilde{\tau})$  given in Fig. 8. The hybrid time delay characteristic pdf  $\rho(t; \tilde{\tau}, \Delta t)$  can be directly calculated by using (45) and the time correlated delay cross-power spectral density  $P_h(t; \tilde{\tau}, \Delta t)$  with (2) and (3). Both theoretical results and measurement data demonstrate a strong agreement in the temporal correlation of the channel. The correlation decreases noticeably with increasing delay. For large delays,  $\tilde{\tau} \rightarrow \infty$ , the delay-dependent characteristic function converges to a Bessel function as described in (53) aligning well with theoretical expectations. Since both the delay-dependent Doppler pdf and delay-dependent, time-variant LSF get wider with increasing delay, the correlation in the  $\Delta t$  variable naturally decreases, as can be seen in Figs. 5 and 6. The influence of the LOS signal and the specular reflection (SR) reflection, which was eliminated from the measurement data for comparison reasons, is still slightly observable for delays  $\tilde{\tau}$  close to  $\tilde{\tau}_{\text{sr}} = 2.1$  according to (15).

Next, we compare the real parts  $\Re$  of the newly introduced time-variant, Doppler-dependent frequency characteristic function  $\varrho(t; \Delta \tilde{f} | \nu)$  with  $P_\varrho(t; \Delta \tilde{f} | \nu)$ . Both functions can only be indirectly obtained by (inverse) Fourier transforms. The time-variant hybrid frequency Doppler characteristic pdf  $\varrho(t; \Delta \tilde{f}, \nu)$  is thus divided by its Doppler spectral density  $p(t; \nu)$ . Therefore the correlation in normalized frequency lag  $\Delta \tilde{f}$

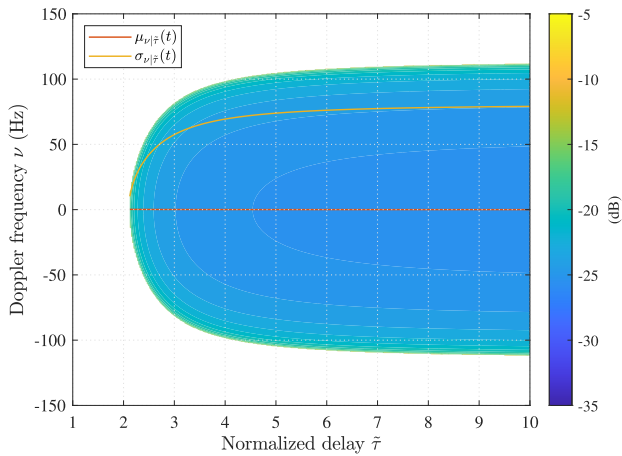


Fig. 5. Theoretical time-variant, delay-dependent Doppler pdf  $p(t; \nu | \bar{\tau})$  with mean Doppler  $\mu_{\nu | \bar{\tau}}(t)$  and Doppler spread  $\sigma_{\nu | \bar{\tau}}(t)$ .

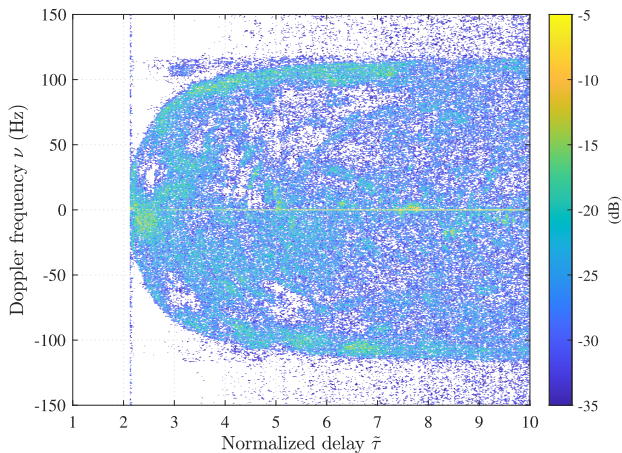


Fig. 6. Measured time-variant, delay-dependent local scattering function  $\mathcal{C}_{\mathbf{H}}(t; \nu | \bar{\tau})$ .

becomes visible. The theoretical results in Fig. 9 show that the correlation is largest for the Doppler frequency  $\nu = 0$  Hz. Both with increasing and decreasing Doppler frequency, the correlation symmetrically diminishes along the normalized frequency axis. The correlation of the measurement data in Fig. 10 shows a similar behavior.

Finally, we compare the joint time frequency characteristic function with the normalized autocorrelation of the time-variant transfer function. The joint time frequency characteristic function  $r(t; \Delta \tilde{f}, \Delta t)$  is obtained by (inverse) Fourier transform from one of the hybrid characteristic pdfs and the autocorrelation of the time-variant transfer function  $R_L(t; \Delta t, \Delta f)$  can be directly calculated from measurement data using (2) and (3). The real parts  $\Re$  of the time-variant joint time frequency characteristic function  $r(t; \Delta \tilde{f}, \Delta t)$  and the time frequency correlation function  $\tilde{R}_L(t; \Delta \tilde{f}, \Delta t)$  are shown in Fig. 11 and Fig. 12. They both have a peak at zero time and zero frequency shift. Along the time and frequency axes, both functions further exhibit the typical decreasing correlation behavior depending on the geometry of the scenario.

After the qualitative analysis of the three conditional and one normalized 2D correlation based and probability based functions, we now verify the presented model with the

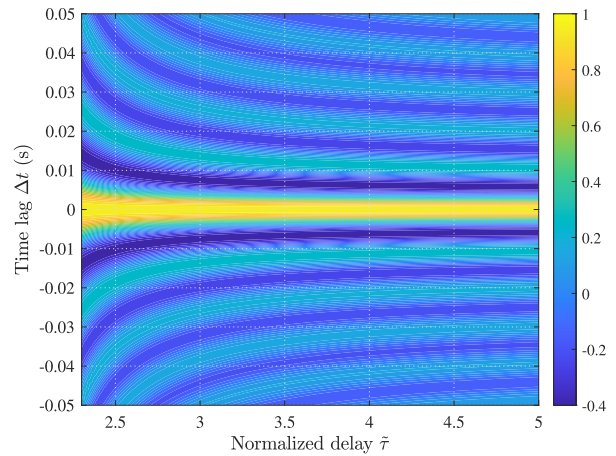


Fig. 7. Theoretical time-variant, delay-dependent temporal characteristic function  $\Re\{\rho(t; \Delta t | \bar{\tau})\}$ .

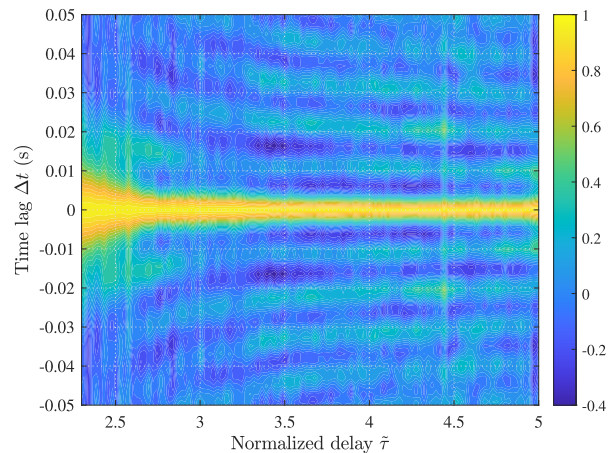


Fig. 8. Measured time-variant, delay-dependent temporal correlation function  $\Re\{P_h(t; \Delta t | \bar{\tau})\}$ .

two validation metrics presented in Section IV-B. Therefore, we use the delay-dependent temporal characteristic function  $\rho(t; \Delta t | \bar{\tau})$  and its delay-dependent correlation based counterpart  $P_h(t; \Delta t | \bar{\tau})$ , since they are the only functions that can be directly calculated from closed-form equations in (45) and (9) or from measurement data with (2), (3), and (25). Due to the linearity of the Fourier transform, the obtained values for the NMSE and the PCC are the same in the other three domains. For the NMSE we obtain a value of 0.47, which shows that the match between our model and the measurements is reasonably accurate, but not perfect due practical constraints like noise and the rather coarse bins. Considering the scattering power is very close to the noise threshold of the channel sounder, such a value is still very good. Similarly, for the PCC we obtain a value of 0.81, which indicates a strong positive linear relationship between model and measurement data. Thus, both metrics confirm the validity of the probability based functions introduced in this paper.

#### D. Full Probability Based Description of a US Channel

In this subsection, we examine the full time-variant 2D probability based description of the US channel. In reference

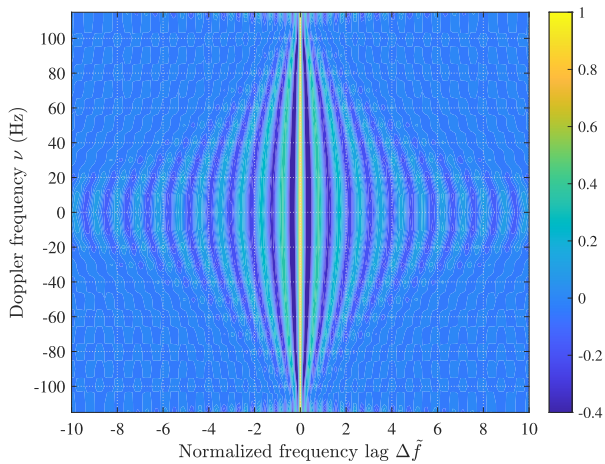


Fig. 9. Theoretical time-variant, Doppler-dependent frequency characteristic function  $\Re \{ \varrho(t; \Delta \tilde{f} | \nu) \}$ .

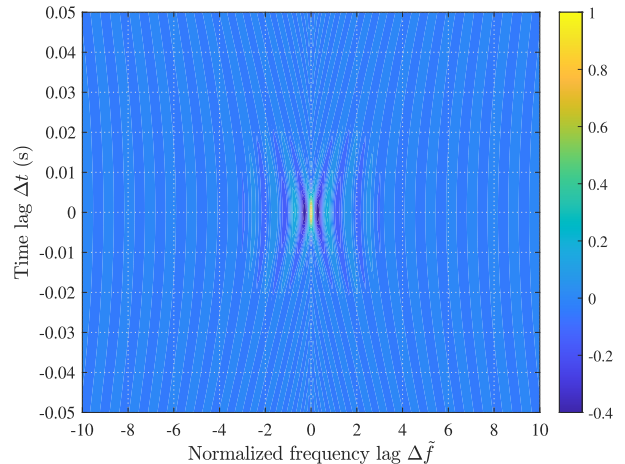


Fig. 11. Theoretical time-variant, joint time frequency characteristic function  $\Re \{ r(t; \Delta \tilde{f}, \Delta t) \}$ .

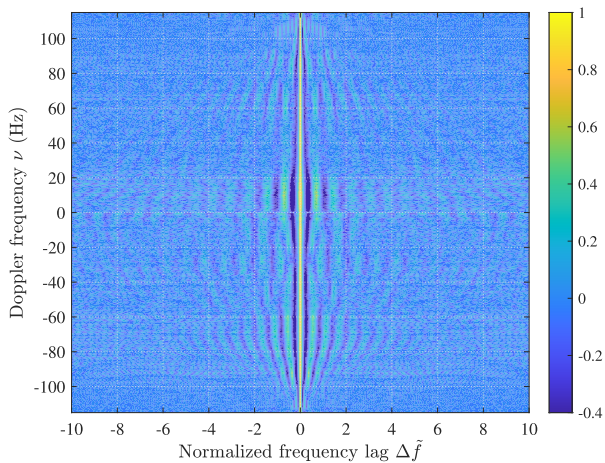


Fig. 10. Measured time-variant, Doppler-dependent frequency correlation function  $\Re \{ P_{\varrho}(t; \Delta \tilde{f} | \nu) \}$ .

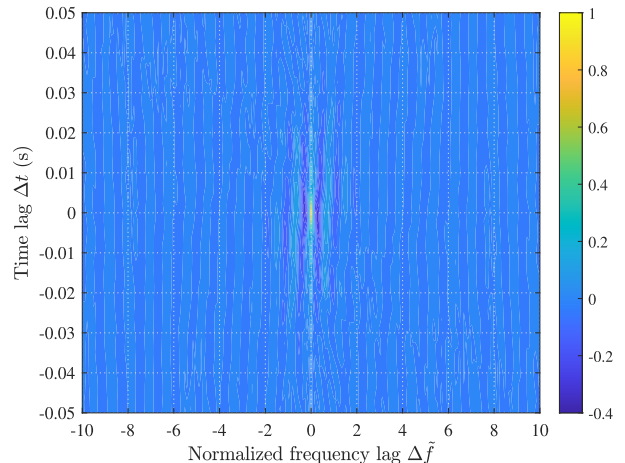


Fig. 12. Measured time-variant, joint time frequency correlation function  $\Re \{ \tilde{R}_L(t; \Delta \tilde{f}, \Delta t) \}$ .

to Fig. 2, the block diagram in Fig. 13 shows the relationship between the different channel descriptions and their corresponding mutual transformations. Furthermore, we compare the normalized one-dimensional (1D) correlation based functions with the probability based functions in Figs. 13(i)-(iv) according to (26) and check their similarity.

We begin with the joint delay Doppler pdf  $p(t; \tilde{\tau}, \nu)$  in Fig. 13(I). Note the similarity to the conditional pdf in Fig. 5. Yet, the key difference is the obvious drop of the probability mass, or equivalently signal power, with increasing delay. This drop of probability with increasing delay, as captured by the marginal  $p(t; \tilde{\tau})$  in Fig. 13(i), is explicitly transferred to the hybrid time delay characteristic pdf  $\rho(t; \tilde{\tau}, \Delta t)$ , see Fig. 13(II). Notably, the joint pdf descriptions correctly account for the weighting of the functions in the delay domain. A comparable weighting occurs in the Doppler domain with the Doppler pdf  $p(t; \nu)$  affecting  $\varrho(t; \Delta \tilde{f}, \nu)$  as shown in Fig. 13(III). Naturally, the joint characteristic function  $r(t; \Delta \tilde{f}, \Delta t)$  in Fig. 13(IV) accounts for both of these weightings implicitly through the Fourier transform.

The clear advantage of these joint descriptions is their compatibility from environmental models and location information of transceivers, as demonstrated in [35]. Moreover, they enable

the calculation of four time-variant marginalized descriptions: the delay pdf  $p(t; \tilde{\tau})$ , the Doppler pdf  $p(t; \nu)$ , as well as the temporal characteristic function  $r(t; \Delta t)$  and the frequency characteristic function  $r(t; \Delta \tilde{f})$  following the properties of pdfs or corresponding characteristic functions. In Fig. 13, the respective relationships of these marginalized descriptions are depicted by arrows.

The time-variant probability densities  $p(t; \tilde{\tau})$  and  $p(t; \nu)$  are computed by integrating the joint delay Doppler pdf  $p(t; \tilde{\tau}, \nu)$  of Fig. 13(I), where the integration variable is  $\nu$  for  $p(t; \tilde{\tau})$  and  $\tilde{\tau}$  for  $p(t; \nu)$ . Alternatively, the same result can be obtained by setting the Delta variables  $\Delta t = 0$  in  $\rho(t; \tilde{\tau}, \Delta t)$ , Fig. 13(II) and  $\Delta \tilde{f} = 0$  in  $\varrho(t; \Delta \tilde{f}, \nu)$ , Fig. 13(III), respectively. This is a general property of a characteristic function. As illustrated in Figs. 13(i)-(ii), the analytically computed pdfs  $p(t; \tilde{\tau})$  and  $p(t; \nu)$  align remarkably well with the two derived from measurement data  $\tilde{P}_h(t; \tilde{\tau})$  and  $\tilde{P}_\rho(t; \nu)$ . Note again, as mentioned above, that in order to reveal the scattering in the channel, the signal components from LOS and SR are eliminated. Therefore, the decreasing behavior of the scatter channel caused by path loss can be clearly observed in Fig. 13(i) and is well reflected by the delay pdf. Regarding the Doppler pdf shown in Fig. 13(ii), it is

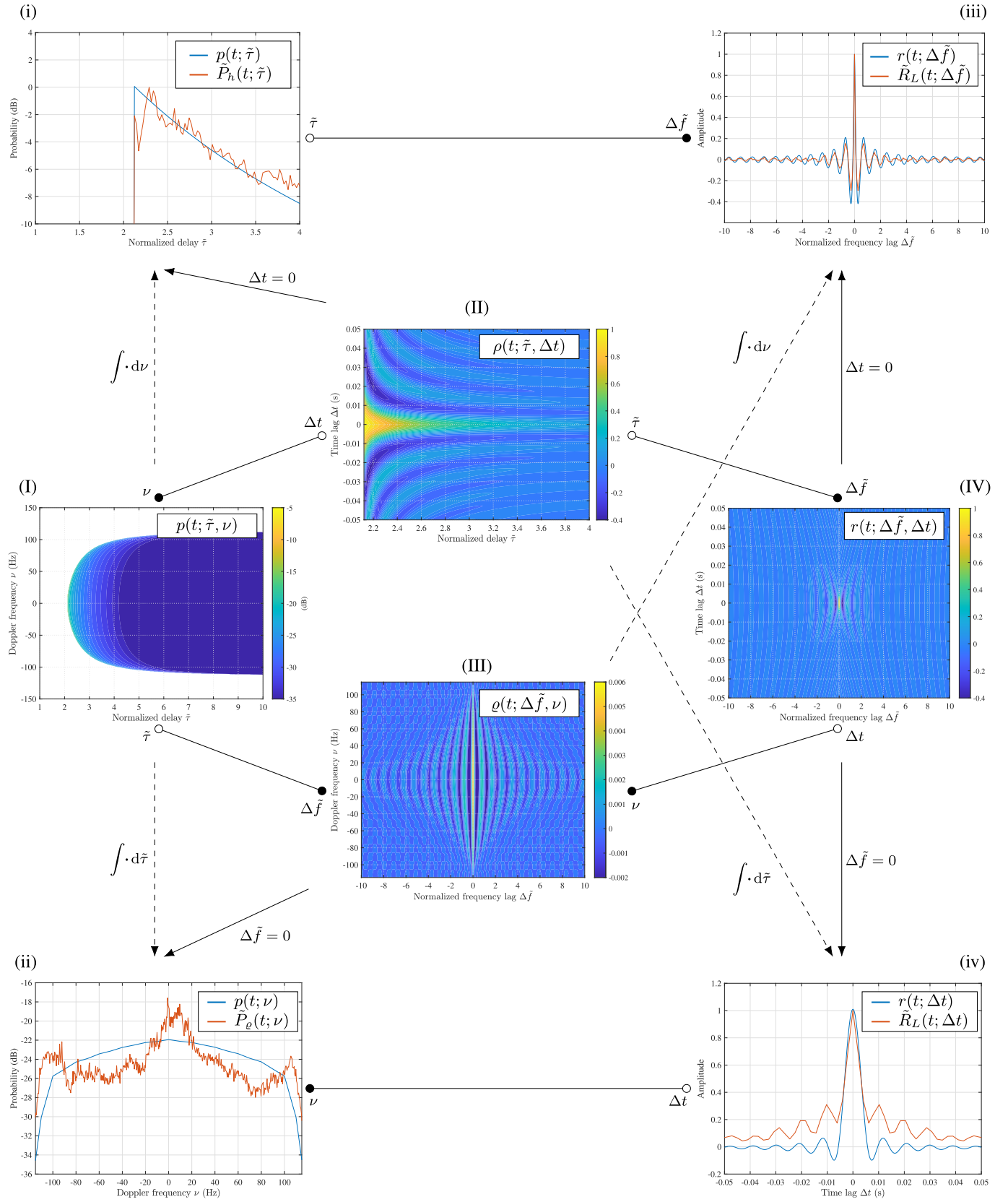


Fig. 13. Time-variant probability based functions of Fig. 2 for the aircraft-to-aircraft scenario described in Sec. IV-A. Calculation of (I) using the closed-form solution provided in [20], (II) using (45) and (50), and (III)-(IV) through corresponding (inverse) Fourier transforms. Calculation of (i)-(iv): The probability based functions (—) are derived from (I)-(IV), following the relationships indicated by the arrows in the diagram. The correlation based functions (—) are computed using equation (2) in combination with (3) and (26) for cases (i), (iii), and (iv). For case (ii), the calculation additionally incorporates equations (4) and (6). Fourier transforms are indicated by the  $\circ \rightarrow \bullet$  sign, integrals by  $- \rightarrow -$ , and setting the  $\Delta$  variable to zero by  $\rightarrow$ .

evident that the shape deviates from the traditional Jakes spectrum. While the theoretical model shows a concave shape, the measurements exhibit a higher probability at zero Doppler due to the imperfect elimination of LOS and SR, along with a slight increase at the limiting Doppler frequencies.

Finally, let us analyze the two time-variant characteristic functions  $r(t; \Delta \tilde{f})$  and  $r(t; \Delta t)$ . The former, shown in Fig. 13(iii), can be obtained via marginalization of the hybrid frequency Doppler characteristic pdf  $\varrho(t; \Delta \tilde{f}, \nu)$  or by setting  $\Delta t = 0$  in  $r(t; \Delta \tilde{f}, \Delta t)$ . The temporal characteristic function, shown in Fig. 13(iv),  $r(t; \Delta t)$  can be similarly computed from  $\rho(t; \tilde{\tau}, \Delta t)$  or  $r(t; \Delta \tilde{f}, \Delta t)$ . We observe that the zero crossings and sidelobes of the theoretical curves closely match the two normalized correlation based functions computed from measurement data  $\tilde{R}_L(t; \Delta \tilde{f})$  and  $\tilde{R}_L(t; \Delta t)$  both in Fig. 13(iii) and Fig. 13(iv). Further, we can determine the coherence bandwidth as a solution to  $\Re \left\{ r(t; \Delta \tilde{f}, \Delta t = 0) \right\} = 1/2$ . The normalized coherence bandwidth is about  $\tilde{B}_C = 0.126$ , which corresponds to a physical bandwidth of  $B_C = 60.239$  kHz. Note that in Fig. 13(iv) the empirical evaluations show a slight elevation of the sidelobes. This discrepancy can again be attributed to the imperfect elimination of the LOS and SR components. Equivalently to the coherence bandwidth, we derive the channel coherence time as a solution to  $\Re \left\{ r(t; \Delta \tilde{f} = 0, \Delta t) \right\} = 1/2$ , resulting in  $T_C = 6.4$  ms.

## V. CONCLUSION

In this work, we presented a complete analytic probability based description of the mobile-to-mobile uncorrelated scatter channel. The proposed theoretical description is based purely on the geometry of the propagation environment and enables the prediction and simulation of such a channel. We provided a theoretical proof of the equivalence of the proposed probability based description and the common correlation based description, as introduced by Bello and Matz.

For a direct comparison with measurement data, we introduced a so-called hybrid characteristic probability density function and derived a closed-form expression. Using measurement data from an aircraft-to-aircraft measurement campaign, we specifically compared the hybrid time delay characteristic probability density function with the time correlated delay cross-power spectral density. Note that this measured channel represents the most general mobile-to-mobile channel, since the transmitter and receiver are arbitrarily located in 3D space. Both the qualitative and quantitative comparison have shown a strong agreement and confirm the equivalence of the proposed probabilistic description with the correlation based description.

Therewith, our proposed probabilistic description complements the correlation based description of Bello and Matz and provides a comprehensive theoretical description of arbitrary mobile-to-mobile uncorrelated scatter channels.

## ACKNOWLEDGMENT

Special thanks go to Rohde & Schwarz GmbH & Co. KG., for providing the aircraft-to-aircraft measurement data. The authors also would like to thank Gerald Matz for the discussion on non-stationary channels.

## REFERENCES

- [1] S. Darbha, S. Konduri, and P. R. Pagilla, "Benefits of V2V communication for autonomous and connected vehicles," *IEEE Trans. Intell. Transp. Syst.*, vol. 20, no. 5, pp. 1954–1963, May 2019.
- [2] S. O. Rice, "Mathematical analysis of random noise," *Bell Syst. Tech. J.*, vol. 23, no. 3, pp. 282–332, Jul. 1944.
- [3] S. O. Rice, "Mathematical analysis of random noise," *Bell Syst. Tech. J.*, vol. 24, no. 1, pp. 46–156, Jan. 1945.
- [4] R. H. Clarke, "A statistical theory of mobile-radio reception," *Bell Syst. Tech. J.*, vol. 47, no. 6, pp. 957–1000, Jul. 1968.
- [5] W. C. Jakes, *Microwave Mobile Communications*. New York, NY, USA: Wiley, 1994.
- [6] P. Bello, "Characterization of randomly time-variant linear channels," *IEEE Trans. Commun.*, vol. COM-11, no. 4, pp. 360–393, Dec. 1963.
- [7] M. Pätzold, B. O. Hogstad, and N. Youssef, "Modeling, analysis, and simulation of MIMO mobile-to-mobile fading channels," *IEEE Trans. Wireless Commun.*, vol. 7, no. 2, pp. 510–520, Feb. 2008.
- [8] A. G. Zajic and G. L. Stuber, "Three-dimensional modeling and simulation of wideband MIMO mobile-to-mobile channels," *IEEE Trans. Wireless Commun.*, vol. 8, no. 3, pp. 1260–1275, Mar. 2009.
- [9] G. Matz, "On non-WSSUS wireless fading channels," *IEEE Trans. Wireless Commun.*, vol. 4, no. 5, pp. 2465–2478, Sep. 2005.
- [10] L. Bernadó, "Non-stationarity in vehicular wireless channels," Ph.D. dissertation, Institut für Nachrichtentechnik und Hochfrequenztechnik, Technische Universität Wien, Vienna, Austria, Apr. 2012.
- [11] M. Walter, D. Shutin, and A. Dammann, "Time-variant Doppler PDFs and characteristic functions for the vehicle-to-vehicle channel," *IEEE Trans. Veh. Technol.*, vol. 66, no. 12, pp. 10748–10763, Dec. 2017.
- [12] P. Hoehner, "A statistical discrete-time model for the WSSUS multipath channel," *IEEE Trans. Veh. Technol.*, vol. 41, no. 4, pp. 461–468, Nov. 1992.
- [13] C. A. Gutiérrez, M. Pätzold, N. M. Ortega, C. A. Azurdia-Meza, and F. M. Maciel-Barboza, "Doppler shift characterization of wideband mobile radio channels," *IEEE Trans. Veh. Technol.*, vol. 68, no. 12, pp. 12375–12380, Dec. 2019.
- [14] M. S. Bartlett, "The characteristic function of a conditional statistic," *J. London Math. Soc.*, vols. s1–13, no. 1, pp. 62–67, Jan. 1938.
- [15] Z. Wei et al., "Orthogonal time-frequency space modulation: A promising next-generation waveform," *IEEE Wireless Commun.*, vol. 28, no. 4, pp. 136–144, Aug. 2021.
- [16] S. Li, J. Yuan, W. Yuan, Z. Wei, B. Bai, and D. W. K. Ng, "Performance analysis of coded OTFS systems over high-mobility channels," *IEEE Trans. Wireless Commun.*, vol. 20, no. 9, pp. 6033–6048, Sep. 2021.
- [17] M. F. Keskin, C. Marcus, O. Eriksson, A. Alvarado, J. Widmer, and H. Wymeersch, "Integrated sensing and communications with MIMO-OTFS: ISI/ICI exploitation and delay-Doppler multiplexing," *IEEE Trans. Wireless Commun.*, vol. 23, no. 8, pp. 10229–10246, Aug. 2024.
- [18] B. Boashash, *Time-Frequency Signal Analysis and Processing: A Comprehensive Reference*, 2nd ed., Amsterdam, The Netherlands: Elsevier, 2015.
- [19] G. Matz, "Characterization of non-WSSUS fading dispersive channels," in *Proc. IEEE Int. Conf. Commun. (ICC)*, vol. 4, Anchorage, AK, USA, May 2003, pp. 2480–2484.
- [20] M. Walter, D. Shutin, M. Schmidhammer, D. W. Matolak, and A. Zajic, "Geometric analysis of the Doppler frequency for general non-stationary 3D mobile-to-mobile channels based on prolate spheroidal coordinates," *IEEE Trans. Veh. Technol.*, vol. 69, no. 10, pp. 10419–10434, Oct. 2020.
- [21] L. Cohen, "Time-frequency distributions—A review," *Proc. IEEE*, vol. 77, no. 7, pp. 941–981, Jul. 1989.
- [22] M. Walter, T. Zemen, and D. Shutin, "Empirical relationship between local scattering function and joint probability density function," in *Proc. IEEE 26th Annu. Int. Symp. Pers., Indoor, Mobile Radio Commun. (PIMRC)*, Hong Kong, Aug. 2015, pp. 542–546.
- [23] A. Papoulis and S. U. Pillai, *Probability, Random Variables, and Stochastic Processes* (McGraw-Hill electrical and electronic engineering series). New York, NY, USA: McGraw-Hill, 2002.
- [24] M. Pätzold, *Mobile Fading Channels*. Chichester, U.K.: Wiley, 2002.
- [25] M. Walter, D. Shutin, and U.-C. Fiebig, "Prolate spheroidal coordinates for modeling Mobile-to-Mobile channels," *IEEE Antennas Wireless Propag. Lett.*, vol. 14, pp. 155–158, 2015.
- [26] D. Bachman, *A Geometric Approach to Differential Forms*. Boston, MA, USA: Birkhäuser, 2012.

- [27] É. Cartan, “Sur certaines expressions différentielles et le problème de pfaff,” *Annales scientifiques de l’École normale supérieure*, vol. 16, pp. 239–332, Jun. 1899.
- [28] C. Misner, K. Thorne, J. Wheeler, and D. Kaiser, *Gravitation*. Princeton, NJ, USA: Princeton Univ. Press, 2017.
- [29] M. Skolnik, *Radar Handbook* (Electronics electrical engineering), 3rd ed., New York, NY, USA: McGraw-Hill, 2008.
- [30] M. Walter, D. Shutin, D. W. Matolak, N. Schneckenburger, T. Wiedemann, and A. Dammann, “Analysis of non-stationary 3D air-to-air channels using the theory of algebraic curves,” *IEEE Trans. Wireless Commun.*, vol. 18, no. 8, pp. 3767–3780, Aug. 2019.
- [31] M. Walter, “Scattering in non-stationary mobile-to-mobile communications channels,” Ph.D. dissertation, Inst. Commun. Eng., Universität Ulm, Ulm, Germany, 2016.
- [32] M. Friese, “Multitone signals with low crest factor,” *IEEE Trans. Commun.*, vol. 45, no. 10, pp. 1338–1344, Oct. 1997.
- [33] T. Jost, “Satellite-to-indoor wave propagation for positioning applications,” Ph.D. dissertation, Dept. Signal Theory Commun., Univ. Vigo, Vigo, Spain, 2013.
- [34] P. Händel, “Understanding normalized mean squared error in power amplifier linearization,” *IEEE Microw. Wireless Compon. Lett.*, vol. 28, no. 11, pp. 1047–1049, Nov. 2018.
- [35] M. A. Bellido-Manganell and M. Walter, “Non-stationary 3D M2M channel modeling and verification with aircraft-to-aircraft, drone-to-drone, vehicle-to-vehicle, and ship-to-ship measurements,” *IEEE Trans. Veh. Technol.*, vol. 73, no. 5, pp. 6045–6060, May 2024.



**Michael Walter** (Senior Member, IEEE) received the Dipl.-Ing. and Dr.-Ing. degrees in electrical engineering from Ulm University, Germany, in 2008 and 2015, respectively.

Since 2009, he has been a member of the scientific staff with the Institute of Communications and Navigation, German Aerospace Center (DLR), Oberpfaffenhofen, Germany, where he gained extensive experience in organizing and conducting several measurement campaigns for vehicular and aeronautical research. He was a Visiting Scholar with the

School of Electrical and Computer Engineering, Georgia Institute of Technology, in 2014. His research interests include wireless communications, modeling of non-stationary mobile-to-mobile channels, and channel coding.

Dr. Walter was a recipient of the IEEE/AIAA David Lubkowski Memorial Award for Advancement in Digital Avionics Best Paper Award of the 29th DASC in 2011. He is the Co-Chair of the IEEE P1944 UAV and V2V Channel Modeling Subgroup and a member of the IEEE VTS Propagation Committee.



**Martin Schmidhammer** (Senior Member, IEEE) received the master’s degree (Hons.) in electrical engineering from the Technical University of Munich (TUM) in 2016 and the Dr.-Ing. (Ph.D.) degree in electrical engineering from Ulm University in 2022.

Since 2016, he has been a member of the scientific staff with the Institute of Communications and Navigation, German Aerospace Center (DLR). His current research focuses on radio propagation and statistical signal processing, with applications

to radio sensing, localization, and tracking. He has received the VDE Award for his master’s thesis in 2016 and the Best Paper Award at 15th EuCAP in 2021.



**Miguel A. Bellido-Manganell** received the B.Sc. degree in telecommunication engineering from the University of Granada in 2014, and the M.Sc. degree in telecommunication engineering from the University of Malaga, Spain, in 2016. In 2016, he joined the Institute of Communications and Navigation, German Aerospace Center (DLR), as a Research Associate. He has participated in multiple measurement campaigns and has a leading role in the 2019 LDACS Flight Campaign. His research interests include channel modeling, physical layer design and digital signal processing in wireless communications, and medium access control in ad hoc networks.



**Thomas Wiedemann** (Member, IEEE) received the bachelor’s and master’s degrees from the Faculty of Mechanical Engineering, Technical University of Munich, in 2012 and 2014, respectively, and the Ph.D. degree in computer science from the Center for Applied Autonomous Sensor Systems (AASS), Orebro University, Sweden, in 2021. He has been a Scientist with the Swarm Exploration Group, Institute of Communications and Navigation, German Aerospace Center (DLR), since 2014. He has also been affiliated as a Post-Doctoral Researcher with the Chair “Perception for Intelligent Systems,” Technical University of Munich, since 2023. His research interests include multi-robot systems, robotic exploration, and gas source localization.



**Dmitry Shutin** (Senior Member, IEEE) received the master’s degree in computer science from Dniepropetrovsk State University, Ukraine, in 2000, and the Ph.D. degree in electrical engineering from Graz University of Technology, Graz, Austria, in 2006.

He was a Teaching Assistant (2001–2006) and an Assistant Professor (2006–2009) with the Signal Processing and Speech Communication Laboratory, Graz University of Technology. From 2009 to 2011, he was a Research Associate with the Department

of Electrical Engineering, Princeton University, Princeton, NJ, USA. Since 2011, he has been with the Institute of Communications and Navigation, German Aerospace Center, where he is currently a Leader of the Swarm Exploration Group. His current research interests include machine learning for signal processing, Bayesian inference, and statistical signal processing over networks. He was a recipient of the Best Student Paper Award at the 2005 IEEE International Conference on Information, Communications and Signal Processing (ICICSP). In 2009, he received the Erwin Schroedinger Research Fellowship. From 2012 to 2014, he acted as a Selected Advisor of the German Air Navigation Service Provider, within the Navigational System Panel of ICAO. He is a Steering Committee Member of IEEE Autonomous Systems Initiative (ASI).